Nano Research

ISSN 1998-0124 CN 11-5974/O4
https://doi.org/10.26599/NR.2026.94909306

Research Article

Ligand-programmed interfacial nucleation enables uniform ferrite-gold core-shell nanostructures

Weipeng Zhang[1], Jieyu Yan[2], Huanyu Zhao[1], Mingfei Pan[1], Yifan Zhao[3], Xuehuan Ding[1], Siyu Lin[1], Jizi Liu[3], Zhirui Guo[4], Jian Xu[5], Yi Chen[6], Kun Han[2](✉), Yiyi Liu[1](✉), Ning Gu[7,3](✉)

[1] Jiangsu Key Laboratory for Biomedical Electromagnetic Precision Theranostics, School of Biomedical Engineering and Informatics, Nanjing Medical University, Nanjing 211166, China

[2] CAS Key Lab of Bio-Medical Diagnostics, Suzhou Institute of Biomedical Engineering and Technology, Chinese Academy of Sciences, Suzhou 215163, China

[3] Nanjing Research Center for Biomedical Electron Microscopy (NRC-BEM), Nanjing Drum Tower Hospital, Medical School, Nanjing University, Nanjing 210093, China

[4] Nanobiotechnology Laboratory, The Second Affiliated Hospital of Nanjing Medical University, Nanjing 210029, China

[5] Department of Laboratory Medicine, The First Affiliated Hospital with Nanjing Medical University, Nanjing 210029, China

[6] Jiangsu Key Laboratory for Biomaterials and Devices, State Key Laboratory of Digital Medical Engineering, School of Biological Science and Medical Engineering, Southeast University, Nanjing 210096, China

[7] Jiangsu Key Laboratory for Cardiovascular Information and Health Engineering Medicine, Nanjing Drum Tower Hospital, Medical School, Nanjing University, Nanjing 210093, China

Nano Res., **Just Accepted Manuscript** • https://doi.org/10.26599/NR.2026.94909306

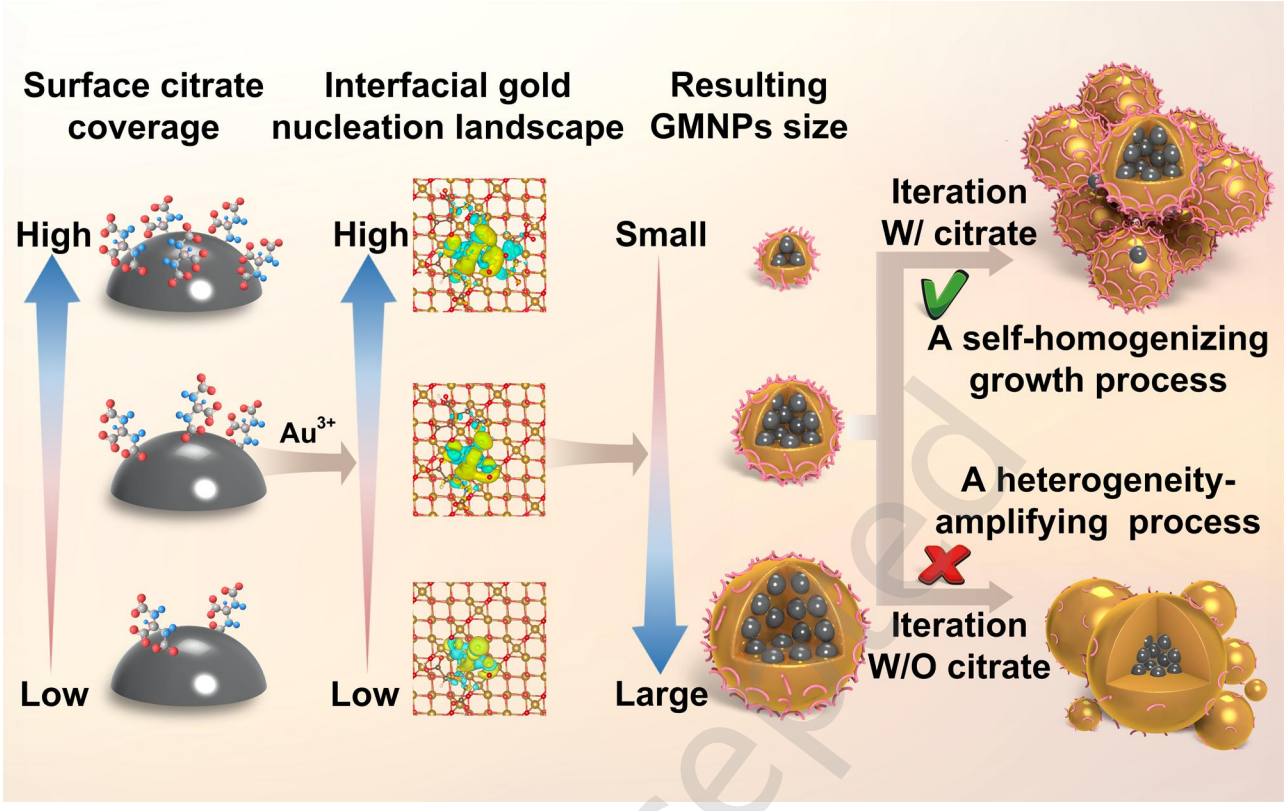
https://www.sciopen.com/journal/1998-0124 on Nov. 2, 2026

© The Authors(s)

Just Accepted

This is a "Just Accepted" manuscript, which has been examined by the peer-review process and has been accepted for publication. A "Just Accepted" manuscript is published online shortly after its acceptance,which is prior to technical editing and formatting and author proofing. Tsinghua University Press (TUP) provides "Just Accepted" as an optional and free service which allows authors to make their results available to the research community as soon as possible after acceptance. After a manuscript has been technically edited and formatted, and the page proofs have been corrected, it will be removed from the "Just Accepted" web site and published officially with volume and article number (e.g., *Nano Research*, **2025**, *18*, 94906990). Please note that technical editing may introduce minor changes to the manuscript text and/or graphics which may affect the content, and all legal disclaimers that apply to the journal pertain. In no event shall TUP be held responsible for errors or consequences arising from the use of any information contained in these "Just Accepted" manuscripts. To cite this anuscript please use its Digital Object Identifier (DOI®),which is identical for all formats of publication.

TABLE OF CONTENTS (TOC)



Surface ligand coverage is used as a molecular programming parameter to control heterogeneous growth at ferrite-gold interfaces. Citrate-dependent precursor-surface interactions redistribute interfacial nucleation and growth, enabling size-controlled nanostructures and, unusually, converting iterative deposition from a heterogeneity-amplifying process into a self-homogenizing growth process. This principle transfers across ferrite compositions and yields functional magnetic-plasmonic nanoprobes.

Just Accepted

Research Article

Ligand-programmed interfacial nucleation enables uniform ferrite-gold core-shell nanostructures

Weipeng Zhang [1], Jieyu Yan [2], Huanyu Zhao [1], Mingfei Pan [1], Yifan Zhao [3], Xuehuan Ding [1], Siyu Lin [1], Jizi Liu [3], Zhirui Guo [4], Jian Xu [5], Yi Chen [6], Kun Han [2] ✉, Yiyi Liu [1] ✉, Ning Gu [7,3] ✉

[1] Jiangsu Key Laboratory for Biomedical Electromagnetic Precision Theranostics, School of Biomedical Engineering and Informatics, Nanjing Medical University, Nanjing 211166, China
[2] CAS Key Lab of Bio-Medical Diagnostics, Suzhou Institute of Biomedical Engineering and Technology, Chinese Academy of Sciences, Suzhou 215163, China
[3] Nanjing Research Center for Biomedical Electron Microscopy (NRC-BEM), Nanjing Drum Tower Hospital, Medical School, Nanjing University, Nanjing 210093, China
[4] Nanobiotechnology Laboratory, The Second Affiliated Hospital of Nanjing Medical University, Nanjing 210029, China
[5] Department of Laboratory Medicine, The First Affiliated Hospital with Nanjing Medical University, Nanjing 210029, China
[6] Jiangsu Key Laboratory for Biomaterials and Devices, State Key Laboratory of Digital Medical Engineering, School of Biological Science and Medical Engineering, Southeast University, Nanjing 210096, China
[7] Jiangsu Key Laboratory for Cardiovascular Information and Health Engineering Medicine, Nanjing Drum Tower Hospital, Medical School, Nanjing University, Nanjing 210093, China

Received: 24 August 2026; **Revised: 29 October 2026**; **Accepted: 2 November 2026**

✉Address correspondence to Kun Han, hank@sibet.ac.cn; Yiyi Liu, yiyi.liu@njmu.edu.cn; Ning Gu, guning@nju.edu.cn

Cite this article: *Nano Research*, 2027, 20, 94909306 https://doi.org/10.26599/NR.2026.94909306

Just Accepted

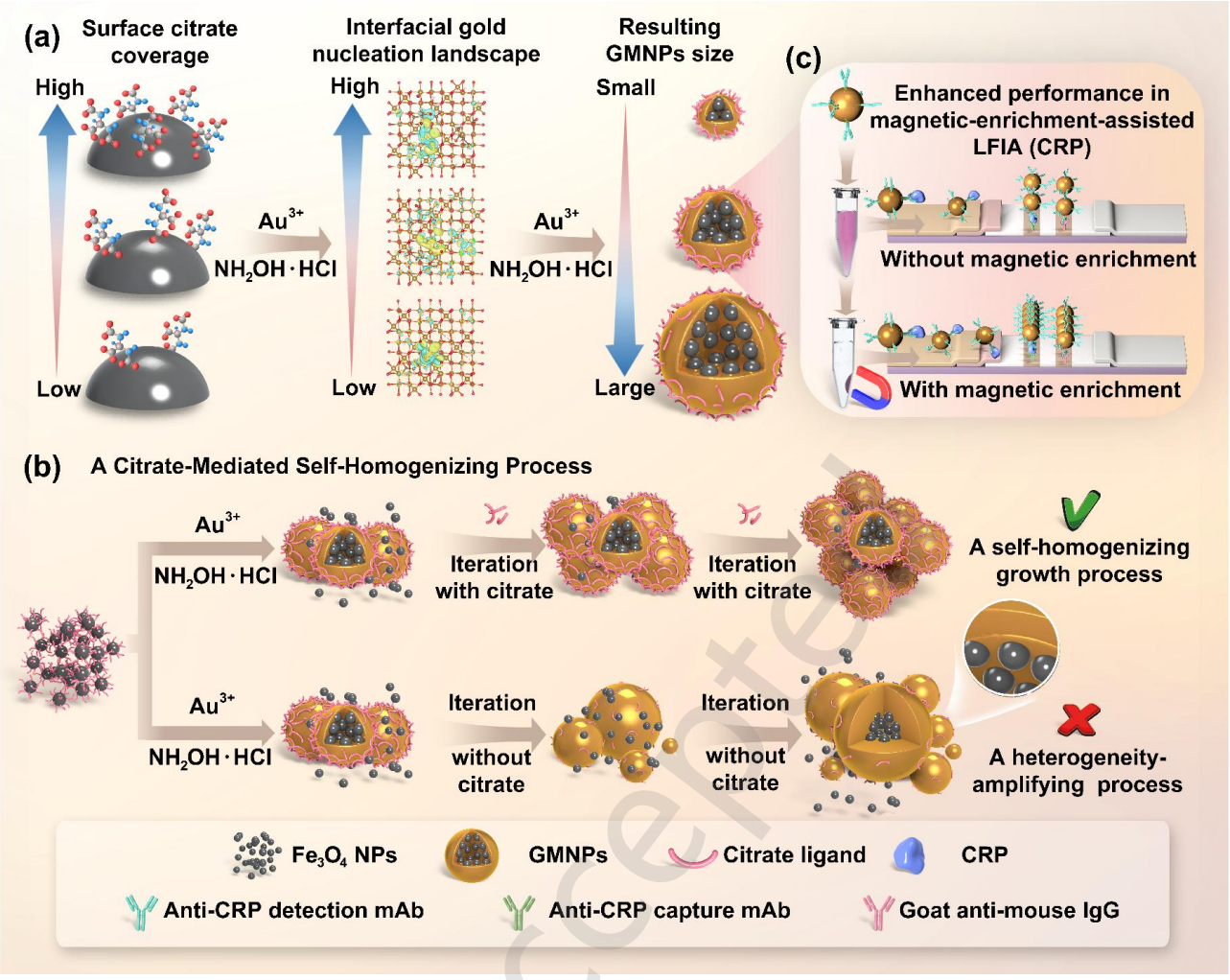
ABSTRACT: Precise control of heterogeneous nucleation at inorganic interfaces is essential for constructing uniform multicomponent nanostructures but remains challenging because nucleation is highly sensitive to local surface chemistry. Here, we demonstrate a ligand-programmed interfacial nucleation strategy for controlling ferrite-gold growth through regulation of surface citrate coverage. Using gold magnetic nanoparticles (GMNPs) composed of Fe_3O_4 and Au as a model system, we show that surface-bound citrate modulates gold precursor adsorption and the heterogeneous nucleation landscape, enabling interlayer-free aqueous synthesis of highly uniform nanostructures with tunable sizes. Notably, citrate transforms iterative gold deposition from a heterogeneity-amplifying process into a self-homogenizing process by suppressing secondary nucleation and excessive growth of pre-existing particles while promoting utilization of residual ferrite nanoparticles. Surface citrate quantification and density functional theory calculations reveal that increasing citrate coverage strengthens interfacial Au-O electronic coupling, charge redistribution, and gold precursor adsorption, providing a molecular basis for the observed growth behavior. The strategy is further validated in $Co_{0.5}Fe_{2.5}O_4$@Au and $Mn_{0.5}Fe_{2.5}O_4$@Au systems. The resulting GMNPs enable a 10-fold sensitivity enhancement over conventional AuNPs-based lateral flow immunoassays following magnetic enrichment. These findings establish surface ligand coverage as a molecular parameter for programming heterogeneous growth at ferrite-gold interfaces.

KEYWORDS: heterogeneous nucleation, surface ligand programming, citrate, ferrite-gold nanostructures, interface chemistry

1 Introduction

Multicomponent core-shell nanoparticles integrate distinct physicochemical properties within a single nanoscale architecture. Among them, ferrite-gold nanostructures, particularly iron oxide nanoparticle (IONP)/gold magnetic nanoparticles (GMNPs), have attracted considerable interest owing to their combination of superparamagnetism, plasmonic activity, and chemically versatile gold surfaces[1, 2]. These characteristics have enabled applications in magnetic separation, biosensing, catalysis, immunoassays, and biomedical diagnosis[3–6]. Their functional performance, however, depends critically on structural uniformity at the single-particle and population levels, including consistent particle dimensions, continuous gold coverage, and minimization of uncoated ferrite nanoparticles and independently nucleated gold nanoparticles (AuNPs). Achieving such uniformity ultimately requires control over heterogeneous nucleation and subsequent growth at core-shell interfaces, as the location and pathway of nucleation can critically determine the structural evolution and final morphology of resulting nanoparticles[7–9].

Current approaches for preparing ferrite-gold core-shell nanostructures can generally be classified into direct and indirect coating strategies. Direct coating deposits gold directly onto magnetic nanoparticle surfaces and provides relatively simple and scalable synthetic routes[10, 11]. However, interfacial nucleation is difficult to regulate, often resulting in incomplete coating, irregular structures, and



Scheme 1. Schematic illustration of the ligand-programmed interfacial nucleation strategy for constructing uniform ferrite-gold core-shell nanostructures. (a) Regulation of gold precursor adsorption, heterogeneous nucleation, and the resulting GMNP sizes through fine-tunning of surface citrate coverage. (b) Comparison of iterative growth processes with and without additional citrate supplementation, respectively. (c) Enhanced performance provided by GMNPs in magnetic-enrichment-assisted lateral flow immunoassays.

coexistence of uncoated magnetic nanoparticles and free AuNPs. Indirect strategies introduce polymeric or inorganic interlayers between the magnetic component and gold shell to improve interfacial compatibility and facilitate gold deposition[12–14]. Although such approaches can enhance coating uniformity, they generally require additional modification steps, organic reagents, or complex preparation procedures. These limitations expose a broader chemical challenge: whether heterogeneous nucleation at an inorganic interface can be programmed directly through molecular regulation of the native surface environment without introducing an artificial intermediate layer[15].

Surface ligands provide a promising pathway for addressing this challenge because ligand coordination and the local interfacial chemical environment can profoundly influence nanoparticle nucleation, crystallization, and subsequent growth[15–19]. Nevertheless, deliberate regulation of surface ligand coverage as a molecular parameter for programming heterogeneous nucleation at pre-existing inorganic interfaces remains comparatively underexplored. Citrate, for example, has long been used in monometallic AuNPs synthesis, where its concentration influences reduction kinetics, particle size, and colloidal stability[20–22]. When metal deposition instead occurs on a pre-existing metal oxide surface, however, the ability of surface-bound ligands to regulate precursor-substrate interactions and thereby alter heterogeneous nucleation remains much less understood. In aqueous systems employing chloroauric acid and hydroxylamine hydrochloride for gold deposition on IONPs[23, 24], citrate is generally regarded as a reducing or stabilizing reagent. Yet citrate contains multiple carboxyl and hydroxyl groups capable of coordinating with unsaturated metal sites on ferrite surfaces[25, 26], potentially modifying the local chemical environment experienced by gold precursor species. This raises a fundamental question: can surface ligand coverage be deliberately programmed to alter precursor-substrate interactions and thereby control the heterogeneous nucleation landscape at ferrite-gold interfaces? Establishing such a relationship would shift control of core-shell growth from structural modification of the interface toward molecular programming of its surface chemistry.

Herein, we demonstrate a citrate-programmed interfacial nucleation strategy for constructing highly uniform ferrite-gold nanostructures. Using Fe_3O_4/Au GMNPs as a model system, we show that citrate coverage on ferrite surfaces acts as a molecular regulatory parameter that controls gold precursor adsorption and redistributes heterogeneous growth across the ferrite population. Higher citrate coverage favors a more spatially distributed interfacial growth landscape and thereby results in smaller GMNPs, whereas

Not Accepted

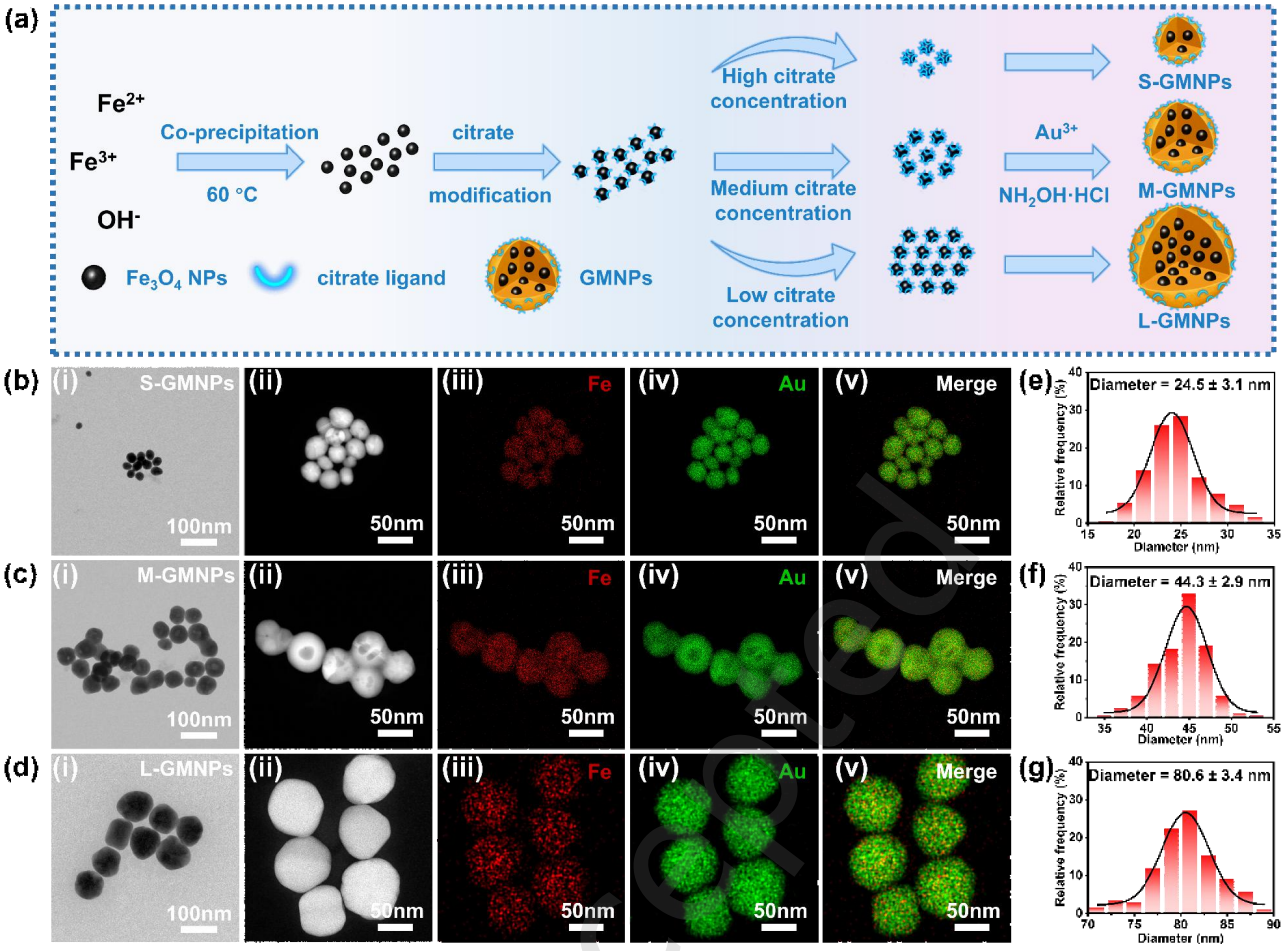


Figure 1. Citrate programs heterogeneous gold nucleation on ferrite surfaces and enables controllable synthesis of uniform GMNPs. (a) Schematic illustration for the preparation of GMNPs with tunable sizes through the "ligand-programmed interfacial nucleation" strategy. (b–d) Representative TEM images, STEM images and the corresponding EDS elemental mapping images of S-, M-, and L-GMNPs. (e–g) Particle size distribution histograms of S-, M-, and L-GMNPs based on measurements of 250 individual nanoparticles, respectively. Curves in these plotting represent Gaussian fits of distribution.

lower citrate coverage results in more localized growth and larger GMNPs (**Scheme 1a**). Remarkably, citrate-mediated interfacial programming transforms iterative gold deposition from a process that normally amplifies structural heterogeneity into a self-homogenizing growth process by suppressing secondary nucleation and excessive enlargement of pre-existing particles while promoting utilization of residual ferrite nanoparticles (**Scheme 1b**). Quantitative measurements of surface citrate coverage, combined with density functional theory (DFT) calculations, reveal that increasing citrate coverage strengthens interfacial Au-O electronic coupling, charge redistribution, and gold precursor adsorption (**Scheme 1a**), providing a molecular basis for ligand-dependent redistribution of heterogeneous growth. Extension to $Co_{0.5}Fe_{2.5}O_4$@Au and $Mn_{0.5}Fe_{2.5}O_4$@Au establishes transferability across ferrite-gold interfaces with different surface chemical environments. Finally, the resulting uniform GMNPs provide enhanced performance in magnetic-enrichment-assisted lateral flow immunoassays (LFIAs) (**Scheme 1c**), illustrating how molecular regulation of interfacial growth can translate into functional magnetic-plasmonic nanostructures.

2 Results and discussion

2.1 Citrate coverage programs heterogeneous gold nucleation at ferrite interfaces

The formation of uniform multicomponent nanostructures is fundamentally governed by the nucleation behavior of the secondary component at the substrate interface. Inspired by the coordination capability of citrate toward metal oxide surfaces, we hypothesized that surface-bound citrate could serve as a molecular regulator of heterogeneous gold nucleation on ferrite nanoparticles. To test this hypothesis, Fe_3O_4 nanoparticles were selected as a model ferrite substrate, and citrate concentration was systematically varied while all other reaction parameters were maintained
unchanged. Fe_3O_4 nanoparticles with an average diameter of 11.7 ± 5.8 nm were first prepared through a coprecipitation method (**Figure S1**). After citrate modification under alkaline conditions (pH 9.5), the resulting Fe_3O_4@citrate nanoparticles were introduced into a hydroxylamine-mediated gold growth system, followed by four iterative coating cycles to generate GMNPs (**Figure 1a**).

Remarkably, varying only the citrate concentration enabled continuous regulation of the dimensions of the resulting GMNPs. Citrate concentrations of 227.27, 159.09, and 22.73 μM yielded three representative products with average diameters of 24.5 ± 3.1, 44.3 ± 2.9, and 80.6 ± 3.4 nm, respectively (**Figure 1b–d**), hereafter denoted as S-GMNPs, M-GMNPs, and L-GMNPs. High-angle annular dark-field scanning transmission electron microscopy (STEM-HAADF) revealed highly uniform spherical morphologies with narrow size distributions across all three samples. Energy-dispersive

Just Accepted

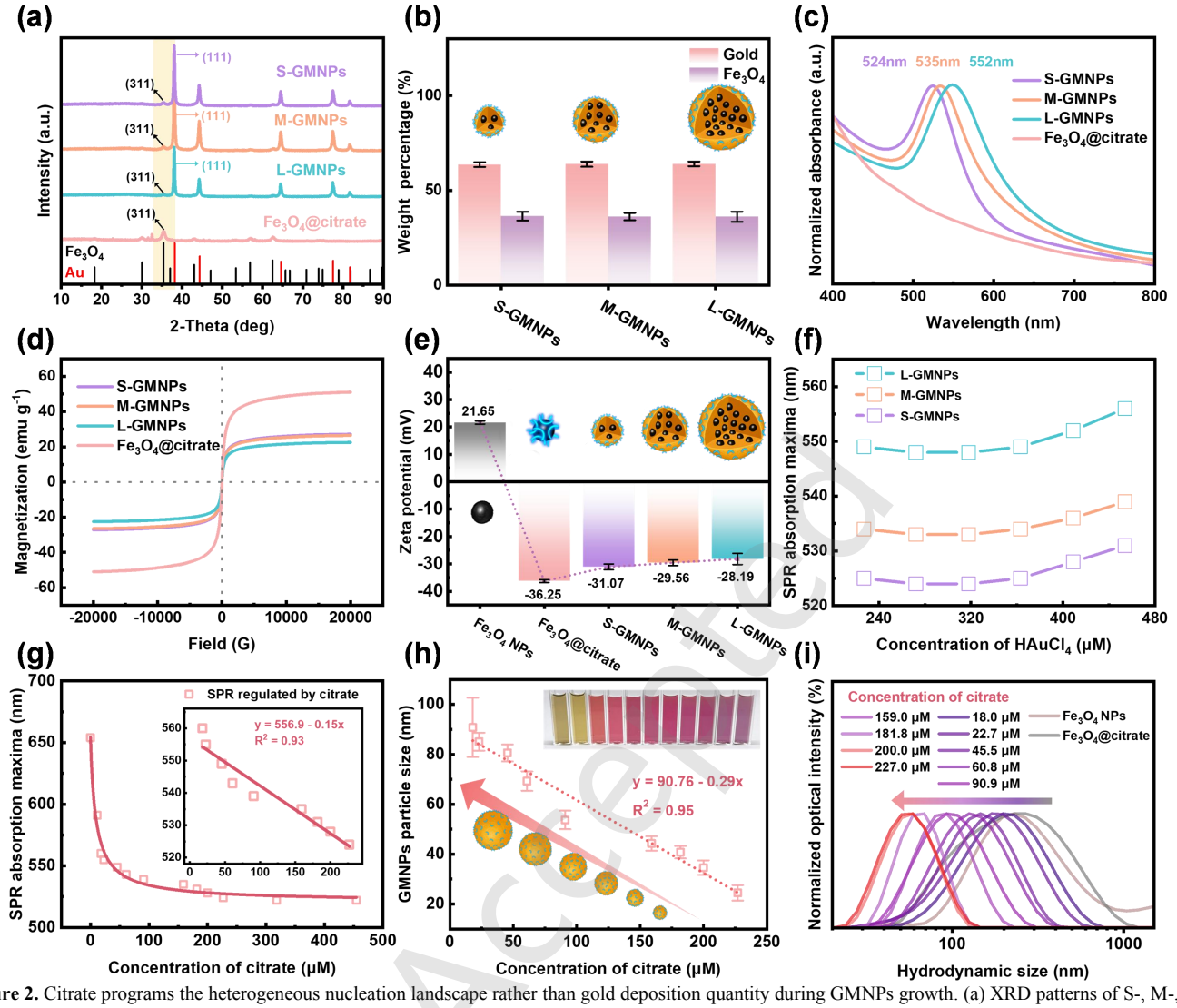


Figure 2. Citrate programs the heterogeneous nucleation landscape rather than gold deposition quantity during GMNPs growth. (a) XRD patterns of S-, M-, and L-GMNPs. (b) Weight percentage of Au and Fe_3O_4 in S-, M-, and L-GMNPs calculated from ICP-MS results. (c) UV–vis absorption spectra of citrate-stabilized S-GMNPs, M-GMNPs, L-GMNPs, and Fe_3O_4 nanoparticles. (d) Field-dependent magnetization curves of S-GMNPs, M-GMNPs, L-GMNPs, and Fe_3O_4 nanoparticles. (e) ζ-potential measurements of Fe_3O_4 nanoparticles, citrate-stabilized Fe_3O_4 nanoparticles, and S-GMNPs, M-GMNPs, and L-GMNPs. (f) Correlations between the LSPR peak positions of S-GMNPs/M-GMNPs/L-GMNPs and $HAuCl_4$ concentrations in the reaction system, respectively. (g) Correlation between the LSPR peak positions of GMNPs and citrate concentrations in the reaction system. Inset shows the linear correlation observed within the citrate concentration range of 23–227 μM, with an $R^2 = 0.93$. (h) The linear correlation between GMNP sizes and citrate concentrations in the reaction system, with an $R^2 = 0.95$. Inset shows the optical images of bare Fe_3O_4 nanoparticles, citrate-stabilized Fe_3O_4 nanoparticles, and 9 GMNP samples with increasing particle sizes (from left to right). (i) Hydrodynamic sizes of GMNPs prepared under different citrate concentrations.

X-ray spectroscopy (EDS) elemental mapping and line-scanning analyses further revealed Fe-rich interiors surrounded by continuous Au-rich regions, confirming formation of ferrite-gold core-shell architectures (**Figure 1b–d and Figure S2**).

Importantly, citrate-dependent size regulation was not accompanied by substantial changes in overall composition. X-ray diffraction (XRD) patterns confirmed characteristic Fe_3O_4 and Au crystalline phases in all three samples (**Figure 2a**). Inductively coupled plasma mass spectrometry (ICP-MS) further revealed nearly invariant Fe/Au mass ratios, with Au contents ranging only from 63.61% to 63.95% among S-, M-, and L-GMNPs (**Figure 2b**). The pronounced variation in particle dimensions despite nearly unchanged Fe/Au composition is inconsistent with a simple growth scenario in which increasingly thick gold shells form around otherwise identical individual ferrite nanoparticles. Instead, the results indicate that citrate alters how ferrite-gold growth is distributed during formation of the final nanostructures rather than simply controlling the total quantity of deposited gold.

Considering the dimensions of the initial ferrite nanoparticles relative to the final GMNPs, incorporation of multiple ferrite nanoparticles within individual GMNPs is plausible, particularly for the larger products, and is consistent with the nearly invariant Fe/Au composition. Because the internal cross-sectional architecture cannot be directly resolved by the present characterization (i.e., ultramicrotomy and focused ion beam) due to the small particle dimensions of GMNPs, however, this interpretation is treated as a structural model rather than a definitive assignment. We have further characterized as-prepared Fe_3O_4 nanoparticles, Fe_3O_4@citrate nanoparticles and samples of M-GMNPs collected at different reaction stages of the initial gold nucleation using both TEM and SEM, trying to intuitively show the corresponding changes. As shown in **Figure S3**, Fe_3O_4@citrate nanoparticles exhibited improved dispersibility and reduced aggregation compared to as-prepared

Accepted

Fe_3O_4 nanoparticles. During the initial gold growth in the hydroxylamine-mediated gold growth system, GMNPs with relatively heterogeneous sizes gradually formed, followed by an increase in the GMNP population and stabilization of particle sizes as the reaction proceeded. Accordingly, the following discussion focuses on the experimentally supported redistribution of heterogeneous ferrite-gold growth without assuming a specific number of ferrite nanoparticles within each final GMNP.

The resulting nanostructures exhibited characteristic size-dependent plasmonic and magnetic properties. Compared with bare Fe_3O_4 nanoparticles, all GMNPs displayed pronounced localized surface plasmon resonance (LSPR) absorption bands that progressively red-shifted with increasing particle size (**Figure 2c**). Previous study has reported similar solid ferrite-gold core-shell nanostructures using hydroxylamine-mediated gold growth strategy[24], while citrate-stabilized AuNPs exhibited size-dependent LSPR shifts which were in good agreement with our GMNPs holding comparable sizes[27]. In addition, electron microscopy showed that monodispersed aggregation-free discrete nanoparticles with smooth particle surfaces were evident for all GMNPs samples, and their UV–vis absorption spectra only exhibited single LSPR peaks without peak splitting or broadening. Taken together, these evidences suggest that the LSPR redshift of GMNPs is mainly attributed to increasing particle sizes rather than interparticle plasmonic coupling. Magnetic measurements confirmed that superparamagnetic behavior was retained after gold deposition, although the saturation magnetization decreased with increasing particle size (**Figure 2d**). Zeta-potential measurements further showed that citrate modification changed the surface potential of Fe_3O_4 nanoparticles from approximately +22 to -36 mV, while the resulting GMNPs maintained stable negative surface potentials of approximately -30 mV (**Figure 2e**). Together, these results establish citrate concentration as an effective parameter for regulating ferrite-gold nanostructure formation. More importantly, the nearly invariant composition across substantially different particle dimensions suggests that citrate controls where and how heterogeneous ferrite-gold growth is distributed, rather than how much gold is ultimately deposited.

2.2 Citrate programs the heterogeneous nucleation landscape rather than gold deposition quantity

To further understand how citrate regulates ferrite-gold growth, we systematically investigated the relationships among citrate concentration, gold precursor availability, and nanoparticle evolution. The LSPR peak positions of S-, M-, and L-GMNPs remained nearly unchanged over a broad $HAuCl_4$ concentration range and began to red-shift only when the precursor concentration exceeded 360 μM (**Figure 2f**). Thus, under citrate-regulated conditions, additional gold precursor does not immediately translate into enlargement of existing GMNPs, suggesting that precursor consumption is governed by the available interfacial growth landscape rather than solely by precursor quantity.

As illustrated in **Figure S4**, the LSPR peak positions showed a gradual red-shift with decreasing citrate concentrations and a clear inverse relationship between the LSPR maxima and citrate concentration can be concluded (**Figure 2g**), whereas the single LSPR band signature was retained across all samples without obvious peak splitting or broadening. Electron microscopy revealed a corresponding decrease in particle dimensions with increasing citrate concentration (**Figure S5**), and particle size correlated strongly with LSPR wavelength (R^2 = 0.98, **Figure S6**). Within the effective citrate-regulation window of 23–227 μM, particle diameter displayed a negative linear dependence on citrate concentration (R^2 = 0.95, **Figure 2h**). Dynamic light scattering measurements further supported this citrate-dependent size evolution (**Figure 2i**).

Control experiments demonstrated that citrate is essential for maintaining a controlled interfacial growth environment. In its absence, gold deposition produced substantially larger particles with irregular petal-like morphologies and broadened, strongly red-shifted plasmonic features (**Figure S7a and b**), consistent with poorly regulated nucleation and growth. Conversely, excessive citrate concentrations (>454 μM) yielded smaller particles but reduced monodispersity, likely because increased ionic strength and changes in the reaction environment begin to interfere with the optimized interfacial growth process (**Figure S7c–f**).

Together with the nearly invariant Fe/Au composition, these observations support a model in which citrate regulates the spatial distribution of heterogeneous nucleation and subsequent growth across the ferrite population, rather than the total quantity of gold deposition. Higher citrate concentrations favor a more spatially distributed interfacial growth landscape, limiting localized evolution into larger composite structures and producing smaller GMNPs. At lower citrate concentrations, heterogeneous growth becomes concentrated within fewer effective growth domains, leading to larger final nanostructures. Citrate therefore acts as an interfacial programming element that regulates the heterogeneous nucleation landscape rather than functioning simply as a stabilizing or reducing reagent.

Successful expression of this ligand-programmed behavior also requires a reaction environment in which precursor reduction proceeds efficiently. Under the optimized alkaline condition (pH 9.5), highly uniform GMNPs were obtained (**Figure S8**). At neutral pH, broader and red-shifted LSPR bands indicated less controlled growth, whereas decreasing the pH to 3.2 nearly abolished gold deposition. This behavior is consistent with the established pH dependence of hydroxylamine-mediated Au(III) reduction[28]. Previous studies have shown that citrate-mediated gold reduction is strongly dependent on pH and is significantly suppressed under highly alkaline conditions at room temperature[29, 30]. This further supported that hydroxylamine hydrochloride serves as the primary reducing agent under the present reaction conditions (25 °C, pH 9.5), whereas citrate mainly acts as a surface ligand, regulating gold precursor adsorption and heterogeneous nucleation at ferrite surfaces. Citrate-mediated interfacial programming therefore operates within a kinetically permissive reduction regime.

Just Accepted

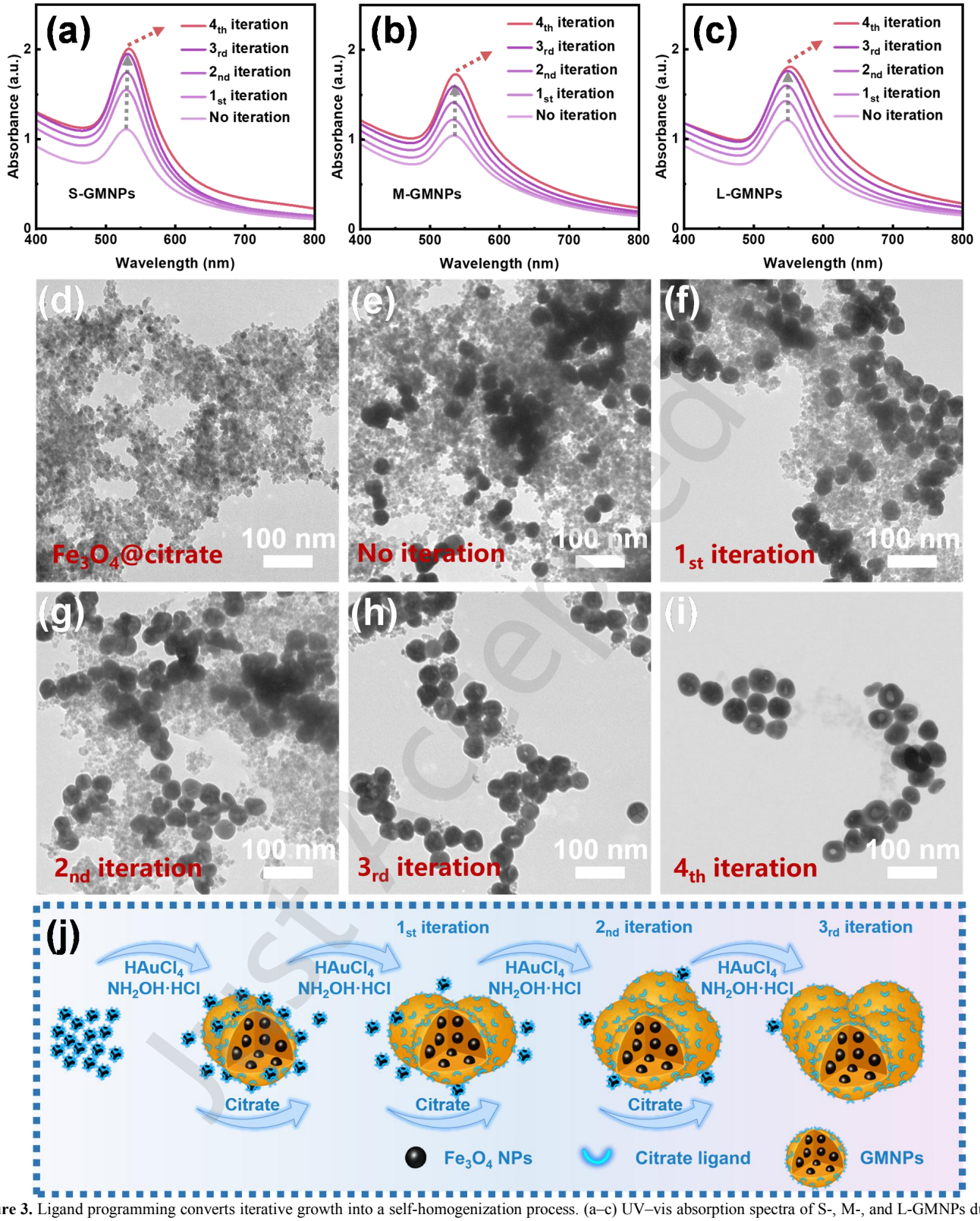


Figure 3. Ligand programming converts iterative growth into a self-homogenization process. (a–c) UV–vis absorption spectra of S-, M-, and L-GMNPs during citrate-mediated iteration process. (d–i) Representative TEM images of M-GMNPs at different stages of citrate-mediated iteration process (scale bar = 100 nm). (j) Proposed schematic illustration for the citrate-mediated iteration process of GMNPs.

2.3 Citrate-mediated interfacial programming converts iterative growth into a self-homogenizing process

A major challenge in ferrite-gold nanoparticle synthesis is that iterative gold deposition often amplifies structural heterogeneity. During conventional iterative growth, nanostructures formed at early stages continue to enlarge while incompletely reacted ferrite nanoparticles persist, ultimately producing mixtures of ferrite-gold particles, exposed magnetic nanoparticles, and independently nucleated AuNPs[4, 31, 32]. Unexpectedly, citrate-mediated growth exhibited fundamentally different behavior. During iterative deposition in the presence of citrate, the LSPR peak positions of S-, M-, and L-GMNPs remained nearly unchanged throughout the first three coating cycles, whereas their absorption intensities continuously increased

Just Accepted

(**Figure 3a–c**). This behavior indicates that newly supplied gold precursor is

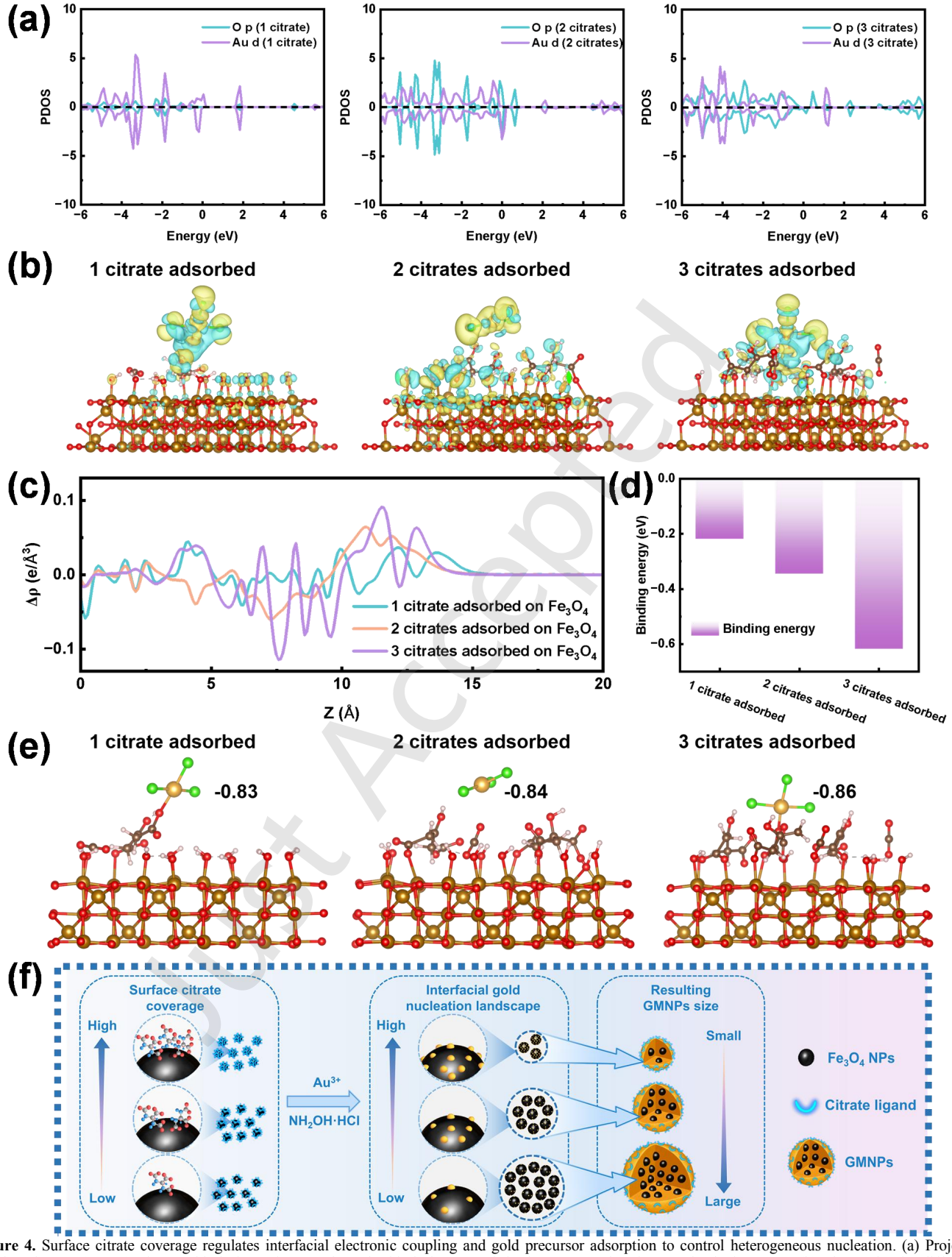


Figure 4. Surface citrate coverage regulates interfacial electronic coupling and gold precursor adsorption to control heterogeneous nucleation. (a) Projected density of states (PDOS) of O p orbitals from citrate and Au d orbitals from $AuCl_3$ in the 1-, 2-, and 3-citrates adsorbed systems. (b) Charge density difference maps of $AuCl_3$ adsorbed on Fe_3O_4 surfaces modified with different numbers of citrate ligands. Yellow and cyan regions represent electron accumulation and depletion, respectively. (c) Plane-averaged charge density difference profiles along the z direction for $AuCl_3$ adsorption on 1-, 2-, and 3-citrates modified Fe_3O_4 surfaces. (d) Calculated binding energies of $AuCl_3$ on Fe_3O_4 surfaces with different citrate adsorption amounts. (e) Bader charge analysis of the interfacial active gold sites in the 1-, 2-, and 3-citrates adsorbed systems. (f) Proposed schematic interpretation of citrate-coverage-dependent gold precursor adsorption, heterogeneous nucleation, and resulting GMNP size based on the DFT results.

Just Accepted

not initially consumed predominantly through enlargement of pre-existing GMNPs, but instead increases the population of Au-containing ferrite-gold nanostructures. However, during the fourth iteration, a noticeable LSPR redshift was observed for S-, M-, and L-GMNPs (**Figure 3a–c**), indicating further enlargement of existing GMNPs. Therefore, the fourth iteration was selected as the termination point for the iterative growth process, and no additional growth cycles were performed.

TEM analysis of M-GMNPs directly visualized this population evolution. Prior to gold deposition, only Fe_3O_4 nanoparticles were observed (**Figure 3d**). After initiation of gold growth, a mixed population of GMNPs and residual Fe_3O_4 nanoparticles emerged (**Figure 3e**). With successive growth cycles, the population of unreacted ferrite nanoparticles progressively decreased while that of GMNPs increased (**Figure 3f–h**). Notably, the characteristic GMNP dimensions remained nearly constant during this stage and increased only after residual Fe_3O_4 nanoparticles were largely consumed (**Figure 3i**), consistent with the corresponding UV–vis spectra (**Figure 3b**).

These observations reveal an unusual evolutionary pathway for iterative heterogeneous growth. Rather than continuously enlarging pre-existing GMNPs, citrate-programmed growth preferentially utilizes residual ferrite nanoparticles, progressively incorporating them into the GMNP population while preserving the dimensions of previously formed particles. Citrate therefore converts iterative deposition from a heterogeneity-amplifying process into a self-homogenizing growth process, in which successive precursor addition reduces rather than magnifies compositional heterogeneity.

Control experiments without citrate further support this interpretation. Iterative coating caused substantial enlargement of Au-containing particles while considerable numbers of unreacted Fe_3O_4 nanoparticles remained (**Figure S9**), resulting in simultaneous increases in size and compositional heterogeneity. We therefore propose that citrate-mediated surface programming suppresses nonspecific secondary nucleation and excessive Au-on-Au growth while maintaining favorable heterogeneous growth at exposed ferrite interfaces (**Figure 3j**). Incoming precursor is preferentially utilized through ferrite-associated growth until the residual ferrite population is depleted, after which further precursor addition increasingly contributes to enlargement of existing GMNPs. This behavior demonstrates that surface ligands can control not only initial formation of multicomponent nanoparticles but also the evolutionary trajectory of heterogeneity during successive growth. The ability to redirect iterative deposition toward progressive population homogenization represents a distinctive consequence of ligand-programmed interfacial nucleation.

2.4 Surface citrate coverage controls interfacial electronic coupling and gold precursor adsorption

The preceding observations suggest that citrate-dependent growth originates from changes in surface ligand coverage rather than simply from bulk citrate concentration. The amount of citrate adsorbed on Fe_3O_4 nanoparticles was therefore quantified by high-performance liquid chromatography coupled with diode-array detection (HPLC–DAD) following acid digestion. A linear calibration curve was obtained for sodium citrate standards (R^2 = 0.99, **Figure S10a**), and characteristic citrate signals were observed at approximately 6.3 min (**Figure S10b**). Surface citrate loading increased approximately linearly with citrate concentration within the effective size-regulation range (**Figure S10c**) and approached a plateau above a feed concentration of 227 μM, indicating near-saturation of available adsorption sites. The correspondence between the citrate-coverage and particle-size-regulation regimes provides experimental evidence that interfacial ligand coverage, rather than bulk citrate concentration alone, is the relevant control parameter.

To investigate how ligand coverage modifies the ferrite-gold interface at the molecular level, DFT calculations were performed using Fe_3O_4 surface models containing different citrate coverages. One-, two-, and three-citrates-modified surfaces represented progressively increasing ligand densities. $AuCl_3$ was employed as a simplified model of an Au(III)-containing precursor to comparatively probe how citrate coverage influences precursor-surface interactions during the initial stage of heterogeneous growth.

Projected density of states (PDOS) analysis revealed overlap between Au d and O p orbitals for all models, consistent with Au-O interfacial interactions (**Figure 4a**). The extent of orbital overlap increased progressively with citrate coverage, with the three-citrates model displaying the most pronounced Au d-O p hybridization. Charge-density-difference calculations similarly showed increasingly pronounced electron redistribution at the Au-O interface with increasing citrate coverage (**Figure 4b**), while plane-averaged charge-density-difference profiles exhibited greater polarization amplitudes for the three-citrates model (**Figure 4c**).

The same trend was reflected in adsorption energetics. Calculated $AuCl_3$ adsorption energies on the one-, two-, and three-citrates-modified Fe_3O_4 surfaces were -0.22, -0.35, and -0.62 eV, respectively (**Figure 4d**), demonstrating progressively more favorable precursor-surface interactions at higher citrate coverages. Bader charge analysis provided a consistent descriptor, showing increased electron accumulation around the interfacial gold atom with increasing citrate coverage (**Figure 4e**).

Collectively, these calculations establish a molecular relationship between surface ligand coverage and precursor-substrate interaction. Increasing citrate coverage strengthens Au-O orbital hybridization, enhances interfacial charge redistribution, and makes adsorption of the modeled Au(III) precursor progressively more favorable. These coverage-dependent interactions provide a molecular basis for the experimentally observed redistribution of heterogeneous ferrite-gold growth. The combined experimental and computational results therefore support a model in which higher citrate coverage creates a more favorable and spatially distributed heterogeneous nucleation landscape across the ferrite population. Stronger precursor affinity at citrate-rich ferrite interfaces promotes widespread interfacial utilization of gold precursor and limits concentration of growth within a smaller number of domains. At lower citrate coverage, less favorable precursor-interface interactions result in a more localized growth landscape and formation of larger GMNPs. This interpretation is consistent with the pronounced citrate-dependent change in particle dimensions despite nearly invariant Fe/Au composition and is schematically summarized in **Figure 4f**. Corresponding

Not Accepted

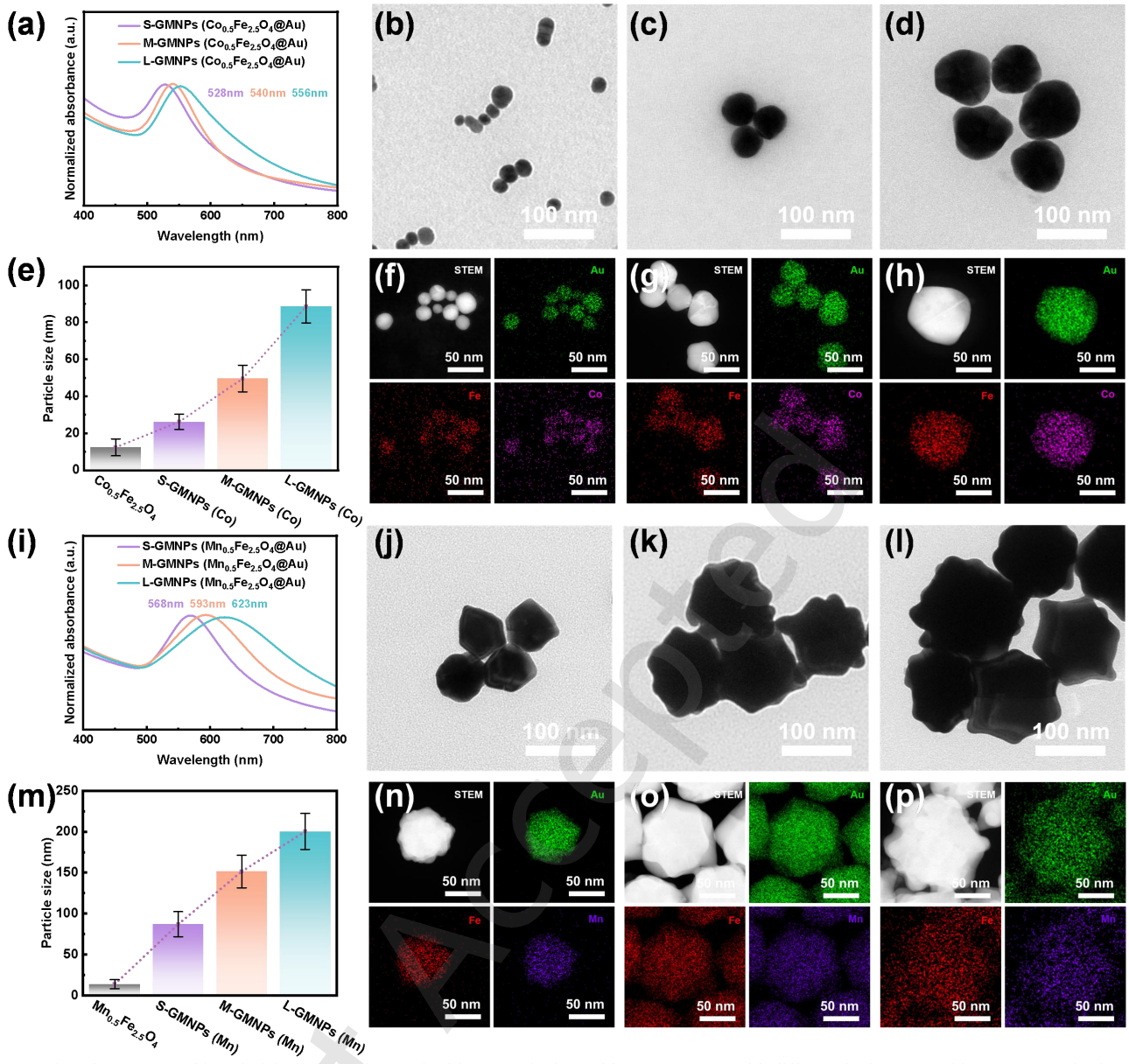


Figure 5. Ligand-programmed interfacial regulation is transferable across ferrite–gold nanostructures with different ferrite compositions. (a) UV–vis absorption spectra of S-, M- and L-GMNPs ($Co_{0.5}Fe_{2.5}O_4$@Au). (b–d) TEM images of S-, M- and L-GMNPs ($Co_{0.5}Fe_{2.5}O_4$@Au), respectively. (e) Particle sizes of $Co_{0.5}Fe_{2.5}O_4$ nanoparticles and S-, M- and L-GMNPs ($Co_{0.5}Fe_{2.5}O_4$@Au). (f–h) STEM-EDS elemental mapping images of S-, M- and L-GMNPs ($Co_{0.5}Fe_{2.5}O_4$@Au), respectively. (i) UV–vis absorption spectra of S-, M- and L-GMNPs ($Mn_{0.5}Fe_{2.5}O_4$@Au). (j–l) TEM images of S-, M- and L-GMNPs ($Mn_{0.5}Fe_{2.5}O_4$@Au), respectively. (m) Particle sizes of $Mn_{0.5}Fe_{2.5}O_4$ nanoparticles and S-, M- and L-GMNPs ($Mn_{0.5}Fe_{2.5}O_4$@Au). (n–p) STEM-EDS elemental mapping images of S-, M- and L-GMNPs ($Mn_{0.5}Fe_{2.5}O_4$@Au), respectively.

top-view models and optimized $AuCl_3$ adsorption configurations are shown in **Figures S11–S12**.

The same molecular picture rationalizes the self-homogenizing behavior observed during iterative deposition. Favorable precursor interactions with exposed citrate-modified ferrite interfaces bias precursor utilization toward residual ferrite nanoparticles rather than excessive growth of pre-existing Au-containing structures, thereby providing a chemical basis for the population evolution observed in **Figure 3**. Citrate thus functions as a molecular programming element that couples surface coverage to precursor adsorption and ultimately to the spatial distribution and evolutionary pathway of heterogeneous ferrite-gold growth.

2.5 Generality of citrate-programmed interfacial regulation across ferrite-gold nanostructures

We next investigated whether the interfacial programming strategy could be transferred to other ferrite compositions. If citrate acts through modulation of precursor adsorption and the interfacial nucleation landscape rather than through a phenomenon unique to Fe_3O_4, analogous regulatory behavior should persist across ferrites retaining related metal-oxygen coordination environments while differing in local surface chemistry. $Co_{0.5}Fe_{2.5}O_4$ and $Mn_{0.5}Fe_{2.5}O_4$ nanoparticles were selected as representative ferrite substrates[33, 34]. For $Co_{0.5}Fe_{2.5}O_4$, decreasing citrate concentration produced progressive red-shifts of the LSPR absorption bands (**Figure 5a**), accompanied by systematic increases in particle dimensions. STEM-HAADF revealed ferrite-gold structures with average diameters of approximately 28.2 ± 4.7, 49.7 ± 9.3, and 88.0 ± 14.5 nm for S-, M-, and L-GMNPs ($Co_{0.5}Fe_{2.5}O_4$@Au), respectively (**Figure 5b–e**), while STEM-

Just Accepted

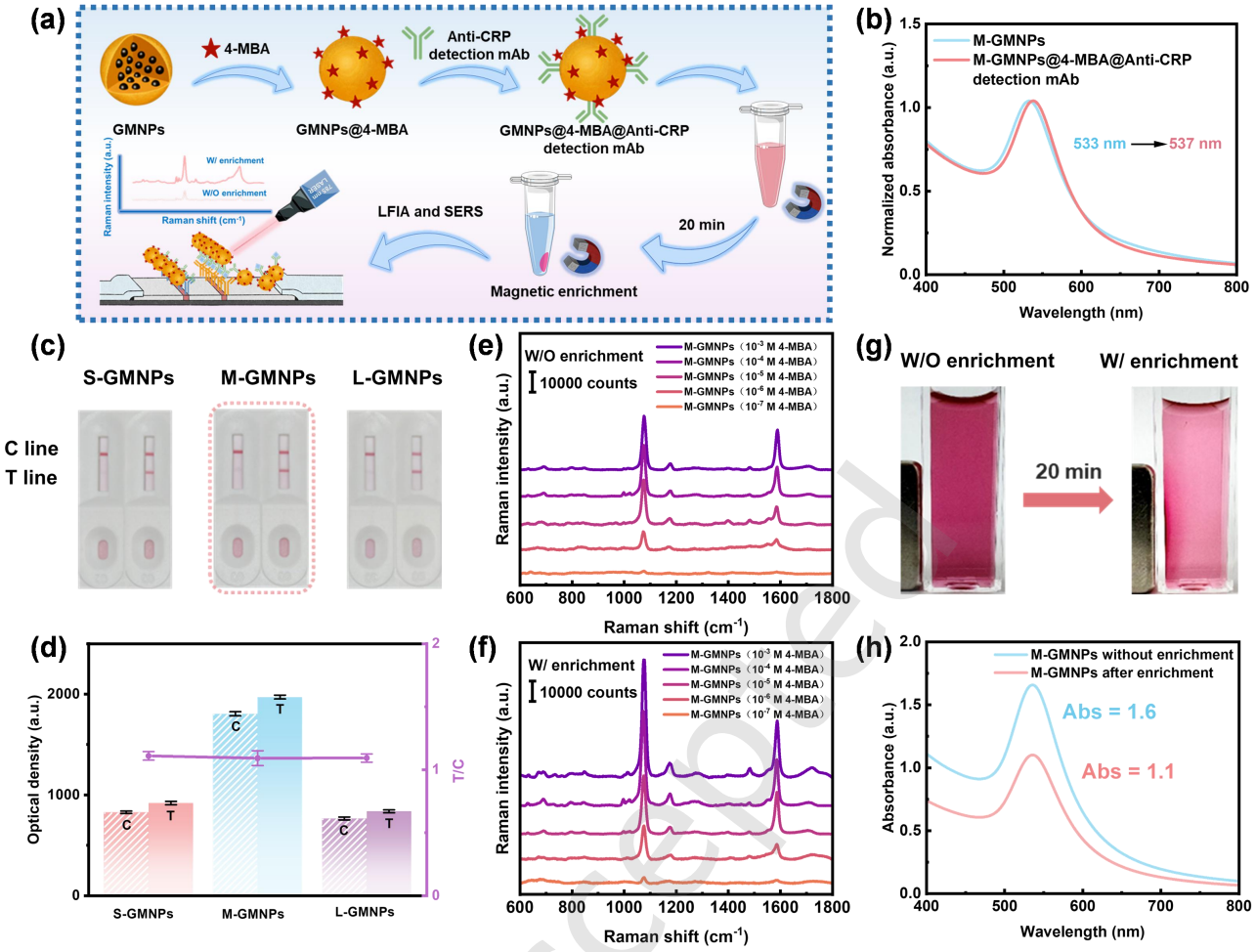


Figure 6. Construction and optimization of ligand-programmed GMNPs for magnetic-enrichment-assisted LFIA. (a) Schematic illustration for the construction of the GMNPs-based colorimetric and SERS dual-mode LFIA platform for CRP detection. (b) UV–vis absorption spectra of M-GMNPs before and after sequential functionalization with 4-MBA Raman reporters and anti-CRP detection mAb. (c) Optical images and (d) quantitative colorimetric responses of S-, M-, and L-GMNPs-based LFIA strips in the detection of CRP. SERS spectra of 4-MBA on M-GMNPs with different loading concentrations (from 10^{-7} to 10^{-3} M) (e) without and (f) after magnetic enrichment under ambient drying conditions. (g) Photographic evidence of the magnetic enrichment efficiency of M-GMNPs. (h) UV–vis absorption spectra of M-GMNPs without and after magnetic enrichment (redispersed in the same volume of deionized water).

EDS mapping confirmed incorporation of Co, Fe, and Au within individual nanostructures (**Figure 5f–h**). The iterative-growth behavior characteristic of Fe_3O_4 was also preserved. During sequential deposition, LSPR intensities continuously increased while peak positions remained nearly unchanged during the initial growth cycles (**Figure S13**), and TEM revealed progressive depletion of residual $Co_{0.5}Fe_{2.5}O_4$ nanoparticles (**Figure S14**). Citrate-mediated suppression of compositional heterogeneity is therefore not unique to Fe_3O_4.

$Mn_{0.5}Fe_{2.5}O_4$ exhibited a similarly citrate-dependent response. Decreasing citrate concentration induced systematic red-shifts of the plasmonic spectra (**Figure 5i**) together with corresponding increases in particle dimensions (**Figure 5j–m**). Unlike the predominantly spherical structures obtained from Fe_3O_4 and $Co_{0.5}Fe_{2.5}O_4$, however, $Mn_{0.5}Fe_{2.5}O_4$-derived products exhibited anisotropic nanostar-like morphologies. STEM-EDS mapping confirmed the presence of Mn, Fe, and Au within these multicomponent structures (**Figure 5n–p**).

This substrate-dependent morphology is mechanistically informative. If citrate functioned primarily as a morphology-directing ligand, comparable structures would be expected across different ferrite compositions. Instead, preservation of citrate-dependent size regulation alongside divergent final morphologies indicates that citrate primarily programs the interfacial nucleation and growth landscape, whereas subsequent structural evolution remains influenced by the intrinsic surface chemistry and crystallographic characteristics of the ferrite substrate, consistent with the broader recognition that substrate surface structure and nucleation pathways are closely coupled in core-shell nanoparticle crystallization[9]. Citrate therefore acts as an interfacial nucleation regulator rather than a universal morphology-directing agent. Taken together, the Fe_3O_4, $Co_{0.5}Fe_{2.5}O_4$ and $Mn_{0.5}Fe_{2.5}O_4$ systems establish transferability of citrate-mediated interfacial programming across chemically distinct ferrite-gold interfaces while demonstrating that programming heterogeneous nucleation does not eliminate substrate-dependent structural evolution.

2.6 Ligand-programmed ferrite-gold nanostructures enable enhanced analytical performance

Having established ligand-programmed interfacial nucleation as a strategy for controlling ferrite-gold growth, we next examined whether the resulting GMNPs could provide functional advantages in a representative analytical platform. Fe_3O_4-based GMNPs were employed as magnetic-

Just Accepted

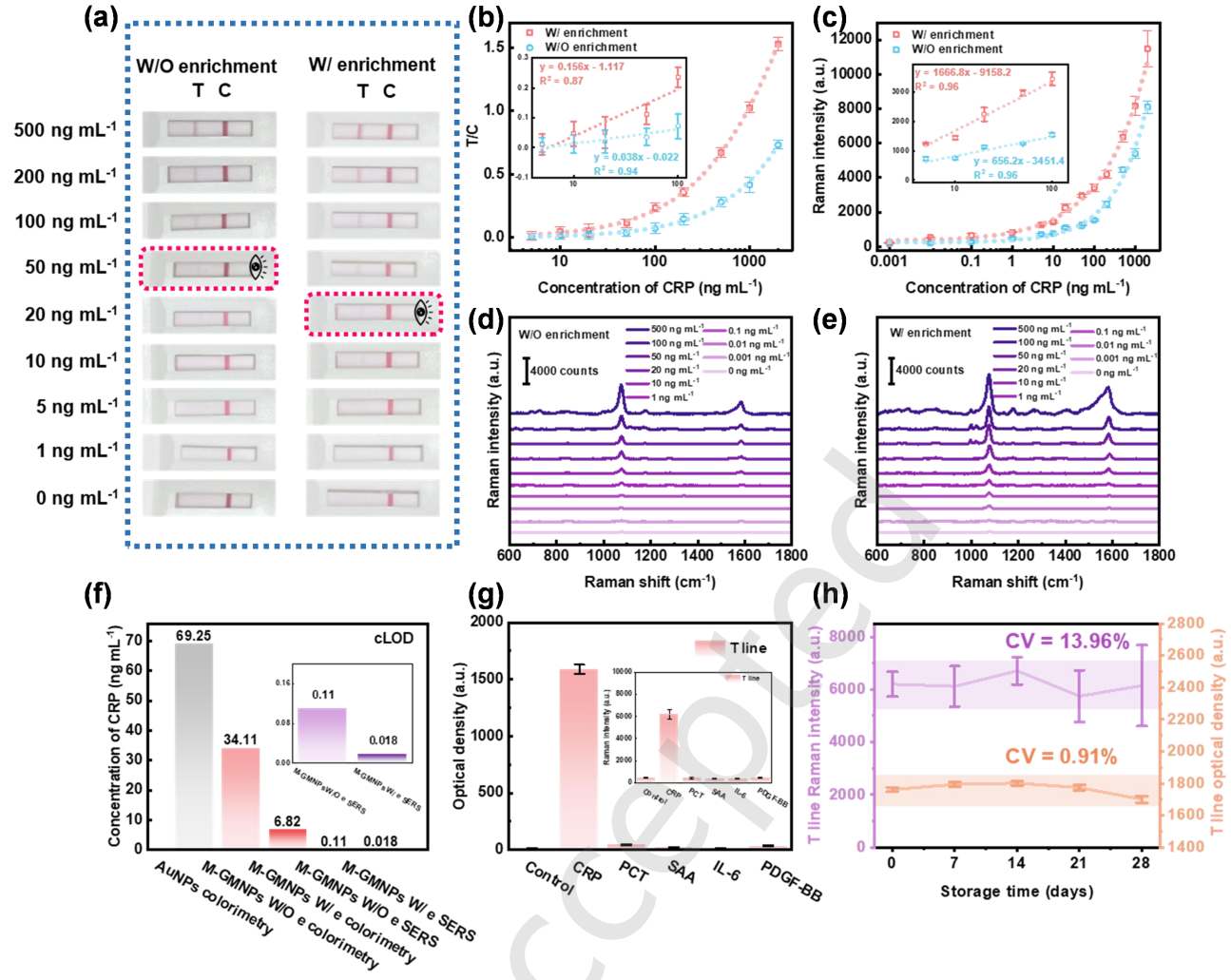


Figure 7. Ligand-programmed GMNPs deliver enhanced analytical performance through improved structural uniformity. (a) Optical images of M-GMNPs-based LFIA strips in the detection of CRP with different concentrations (from 0 ng mL^{-1} to 500 ng mL^{-1}) without (left panel) and after (right panel) magnetic enrichment. (b) Calibration curves for CRP detection based on the T/C values of M-GMNPs without and after magnetic enrichment. Each T/C value represents the averaged values of 3 randomly collected results at given concentration. Inset shows the linear relationships between T/C values and CRP concentrations in the range of 5–100 ng mL^{-1} under both conditions, with R^2 values of 0.94 (without enrichment) and 0.87 (after enrichment), respectively. (c) Calibration curves for CRP detection based on the SERS signals collected at the T line without and after magnetic enrichment. SERS signals represent the averaged values of 10 randomly selected spots at the T line. Inset shows the linear relationships between SERS intensities and CRP concentrations in the range of 5–100 ng mL^{-1} under both conditions, with R^2 values of 0.96 for both cases. Representative SERS spectra collected at the T line of GMNPs-based LFIA strips (d) without and (e) after magnetic enrichment. (f) Calculated limits of detection (cLODs) for AuNPs-based LFIA, colorimetric mode of M-GMNPs-based LFIA (without and after magnetic enrichment), and SERS mode of M-GMNPs-based LFIA (without and after magnetic enrichment). The cLODs for both the colorimetric and SERS modes were determined as 3σ m^{-1}, where σ is the corresponding standard deviation of the blank and m is the corresponding slope of the calibration curve for each case, respectively. (g) Specificity evaluations of M-GMNPs-based LFIA for CRP detection in colorimetric mode and SERS mode (inset). (h) Time-dependent stability of colorimetric and SERS signals at the T line for M-GMNPs-based LFIA strips (measured at 0, 7, 14, 21, and 28 days). Colorimetric signals represent the averaged values of 3 randomly selected spots at the T line during each measurement. SERS signals represent the averaged values of 10 randomly selected spots at the T line during each measurement.

plasmonic nanoprobes in an LFIA for C-reactive protein (CRP), a clinically important biomarker associated with inflammation and infection[35–40]. Their Au-rich exterior enables optical readout and biomolecular functionalization,
whereas the ferrite-containing component enables magnetic target enrichment before analysis.

A dual-mode colorimetric and surface-enhanced Raman scattering (SERS) LFIA was constructed using 4-mercaptobenzoic acid (4-MBA) as the Raman reporter and anti-CRP antibodies as recognition elements (**Figure 6a**). The GMNPs retained colloidal stability during sequential modification with 4-MBA and antibodies, with only minor changes in their LSPR spectra after functionalization (**Figure 6b**). Among the three particle sizes, M-GMNPs generated the strongest assay response (**Figure 6c and d**) and were selected for subsequent studies. Probe preparation and assay conditions were optimized as detailed in **Figure 6e and Figures S15–S16**. Magnetic manipulation enabled efficient concentration of target-bound probes before LFIA analysis (**Figure 6f**), with approximately 69% of nanoparticles recovered after 20 min of magnetic enrichment (**Figure 6g and h and Supporting Movie 1**).

The GMNPs-based LFIA achieved a visible limit of detection (vLOD) of 50 ng mL^{-1} for CRP, which improved to 20 ng mL^{-1} following magnetic enrichment, compared with approximately 200 ng mL^{-1} for conventional AuNPs-based LFIA (**Figure 7a**). Quantitative colorimetric analysis yielded calculated limits of detection (cLODs) of 34.11 and 6.82 ng mL^{-1} before and after magnetic enrichment, respectively, compared with 69.25 ng mL^{-1} for conventional AuNPs reporters (**Figure 7b and Figure S17**).

Just Accepted

The Au-rich surface additionally enabled SERS detection using 4-MBA. The characteristic Raman band at 1075 cm^{-1} increased systematically with CRP concentration (**Figure 7c–e**)[41], yielding SERS-based cLODs of 0.11 ng mL^{-1} without enrichment and 0.018 ng mL^{-1} after magnetic enrichment (**Figure 7f**). The assay also exhibited high specificity against procalcitonin (PCT), serum amyloid A (SAA), platelet-derived growth factor-BB (PDGF-BB), and interleukin-6 (IL-6) (**Figure 7g and Figure S18**) and maintained stable analytical performance during prolonged storage (**Figure 7h and Figure S19**).

These results demonstrate that ligand-programmed ferrite-gold nanostructures can function effectively as magnetic-plasmonic nanoprobes and that their magnetic component provides a substantial analytical advantage through target enrichment. More broadly, the LFIA provides functional validation that precise molecular control of interfacial growth can generate structurally uniform multicomponent nanoparticles suitable for downstream applications. The central significance of the present system therefore lies not in the assay itself, but in the connection between molecular regulation of the ferrite-gold interface and the construction of reproducible functional nanostructures.

3 Conclusion

In summary, we demonstrate that surface ligand coverage can serve as a molecular programming parameter for controlling heterogeneous growth at ferrite-gold interfaces. Quantitative citrate measurements establish the relationship between solution citrate concentration and interfacial ligand coverage, while DFT calculations show that increasing coverage strengthens Au-O electronic coupling, interfacial charge redistribution, and adsorption of the modeled Au(III) precursor. These coverage-dependent interactions provide a molecular basis for the experimentally observed redistribution of ferrite-gold growth and the formation of highly uniform nanostructures with tunable dimensions. A distinctive consequence of this interfacial programming is that iterative gold deposition becomes a self-homogenizing growth process. Citrate-mediated regulation favors utilization of residual ferrite interfaces while suppressing secondary nucleation and excessive enlargement of pre-existing particles, allowing successive deposition to reduce rather than amplify population heterogeneity. Extension to Fe_3O_4, $Co_{0.5}Fe_{2.5}O_4$, and $Mn_{0.5}Fe_{2.5}O_4$ demonstrates transferability across different ferrite compositions, while substrate-dependent morphologies show that ligand-programmed nucleation can coexist with intrinsic structural characteristics of the underlying ferrite. The resulting GMNPs further function as effective magnetic-plasmonic nanoprobes in magnetic-enrichment-assisted LFIA. Collectively, these findings establish ligand coverage as an effective molecular handle for coupling precursor-substrate interactions to heterogeneous nucleation and growth, providing a strategy for engineering structurally uniform multicomponent nanomaterials through interface chemistry.

4 Method

4.1 Materials

Gold(III) chloride trihydrate ($HAuCl_4 \cdot 3H_2O$, ≥99.9%), bovine serum albumin (BSA, ≥98%) and Tween 20 were purchased from Sigma-Aldrich. Iron(III) chloride hexahydrate ($FeCl_3 \cdot 6H_2O$, ≥98%), iron(II) chloride tetrahydrate ($FeCl_2 \cdot 4H_2O$, ≥98%), cobalt(II) chloride hexahydrate ($CoCl_2 \cdot 6H_2O$, ≥98%, ACS grade), manganese(II) chloride tetrahydrate ($MnCl_2 \cdot 4H_2O$, ≥99%, AR grade), methanol (CH_3OH, ≥99.9%), sodium dihydrogen phosphate (NaH_2PO_4, ≥99%, AR grade), phosphoric acid (H_3PO_4, 85%, HPLC grade), ammonia solution ($NH_3 \cdot H_2O$, 28%), hydroxylammonium chloride ($NH_2OH \cdot HCl$, ACS grade), sodium citrate tribasic dihydrate ($C_6H_5Na_3O_7 \cdot 2H_2O$, ≥99%), 4-mercaptobenzoic acid (4-MBA, ≥99%), disodium hydrogen phosphate dodecahydrate ($Na_2HPO_4 \cdot 12H_2O$, ≥99%), potassium chloride (KCl, ≥99%), sodium chloride (NaCl, ≥99%), potassium dihydrogen phosphate (KH_2PO_4, ≥99%), sodium bicarbonate ($NaHCO_3$, ≥99%), sodium carbonate (Na_2CO_3, ≥99%) and polyethylene glycol 6000 (PEG 6000) were purchased from Aladdin. Hydrochloric acid (HCl, 36%, AR grade) were purchased from Shanghai Lingfeng Chemical Reagent Co., Ltd. Sodium azide (NaN_3, ≥99%), sucrose ($C_{12}H_{22}O_{11}$, ≥99%) and sorbitol ($C_6H_{14}O_6$, ≥99%) were purchased from Beijing Bailingwei Technology Co., Ltd. Sodium hydroxide (NaOH, ≥96%) was purchased from Xilong Scientific. CRP calibrator, procalcitonin (PCT), interleukin-6 (IL-6), serum amyloid A (SAA), platelet-derived growth factor-BB (PDGF-BB), anti-CRP detection monoclonal antibodies (anti-CRP detection mAb), anti-CRP capture monoclonal antibodies (anti-CRP capture mAb) and goat anti-mouse IgG were purchased from MEDIX. Nitrocellulose (NC) membranes, polyvinyl chloride (PVC) backing cards, absorbent pads and sample pads were purchased from Wuhan Siree Kechuang Technology Co., Ltd. All chemicals were used as received without further purification. Deionized water was used in all aqueous solutions. All glassware used in the GMNPs and AuNPs synthesis procedures was cleaned in a bath of freshly prepared aqua regia and was rinsed thoroughly in deionized water prior to use.

4.2 Characterization

UV–vis spectra were collected using an Agilent Cary 5000 UV–Vis–NIR spectrophotometer. TEM images were captured using a Thermo Scientific Talos F200X G2 transmission electron microscope operating at 200 kV and a HITACHI HT7800 transmission electron microscope operating at 80 kV. SEM images were obtained by a Thermo Scientific Quattro S scanning electron microscope operating at 20 kV. Dynamic light scattering (DLS) and ζ-potential measurements were performed at 25 °C by using a Malvern Zetasizer Pro ZSU3200 instrument. X-ray di raction (XRD) patterns were collected on a Rigaku SmartLab SE (Japan). Magnetic hysteresis measurements were performed at room temperature using an 8600 Series Vibrating Sample Magnetometer (Lake Shore Cryotronics, USA). Inductively coupled plasma mass spectrometry (ICP-MS) measurements were performed using an Agilent 7850 ICP-MS (USA). HPLC–DAD measurements were performed using an Agilent 1290 Infinity II ultra-high-performance liquid chromatography system equipped with a diode array detector. All SERS spectra were recorded using a HORIBA XploRA PLUS microRaman Spectrometer with the excitation laser wavelength of 785 nm, a laser power of 10 mW and an integration time of 15 s. The syringe pump (model: BYZ-810T) was purchased from Hunan Beyond Medical Technology Co., Ltd. The membrane gold-spraying instrument (HGS510), strip-cutting machine (HGS201), and portable

Just Accepted

immunochromatographic strip reader (FIC-H1) were purchased from Hangzhou Fenghang Technology Co., Ltd.

4.3 Synthesis and preparation of materials

4.3.1 Synthesis of magnetic core nanoparticles

Fe_3O_4, $Co_{0.5}Fe_{2.5}O_4$, and $Mn_{0.5}Fe_{2.5}O_4$ magnetic core nanoparticles were synthesized using a similar co-precipitation method[42]. Briefly, for the synthesis of Fe_3O_4 nanoparticles, 400 mg of $FeCl_3·6H_2O$ (1.48 mmol) and 200 mg of $FeCl_2·4H_2O$ (1.01 mmol) were dissolved in 50 mL of deionized water and heated in a 60 °C water bath under vigorous stirring with N_2 protection. For the synthesis of $Co_{0.5}Fe_{2.5}O_4$ nanoparticles, $FeCl_2·4H_2O$ was partially replaced with $CoCl_2·6H_2O$ at a preset molar ratio to introduce Co into the ferrite lattice. Similarly, $Mn_{0.5}Fe_{2.5}O_4$ nanoparticles were synthesized by replacing the corresponding amount of $FeCl_2·4H_2O$ with $MnCl_2·4H_2O$. Then, 5 mL of 28% ammonia solution was added dropwise at a rate of 600 mL h^{-1} using a syringe pump, and the mixture was incubated for 20 min. The reaction solution gradually turned from transparent yellow to glossy black, indicating the formation of magnetic core nanoparticles. After completion, the product was collected by magnetic separation, washed twice with 50 mL of deionized water, and then redispersed in 50 mL of deionized water.

4.3.2 Preparation of magnetic core@citrate

The obtained magnetic core nanoparticles were incubated with 10 mL of 0.01 M citrate solution under stirring for 2 h, and the resulting black suspension was aged at 4 °C for one week. Subsequently, 4 mL of the aged magnetic core nanoparticles were collected by magnetic separation, redispersed in 20 mL of deionized water, and further subjected to ligand adsorption with 20 mL of 0.1 M citrate solution under continuous stirring for 24 h. The nanoparticles were then washed and redispersed in 40 mL of deionized water to obtain citrate-modified magnetic core nanoparticles, including Fe_3O_4@citrate, $Co_{0.5}Fe_{2.5}O_4$@citrate, and $Mn_{0.5}Fe_{2.5}O_4$@citrate. To prevent oxidation of the magnetic core nanoparticles, the entire process was conducted under N_2 protection.

4.3.3 Size-controlled synthesis of GMNPs

The size-controlled synthesis of GMNPs was adapted from previously reported protocols with modifications[23, 24, 43]. For the synthesis of M-GMNPs, 2 mL of citrate-modified magnetic core nanoparticles were collected by magnetic separation and diluted to 55 mL with deionized water. The mixture was heated in a 25 °C water bath under vigorous stirring, followed by the addition of 350 μL of 25 mM citrate and further stirring for 10 min (initial citrate concentration: 159.09 μM). Next, 500 μL of 25 mM $HAuCl_4$ was added, and the pH was adjusted to weakly alkaline (9.5–10) using NaOH. Afterwards, 500 μL of freshly prepared 0.4 M hydroxylamine hydrochloride solution was introduced, during which the solution color changed from yellow-brown to bluish purple and finally to wine red. For the iterative growth, four additions of 70 μL of 25 mM citrate, 100 μL of 25 mM $HAuCl_4$, and 100 μL of 0.4 M hydroxylamine hydrochloride were performed at 10 min intervals. The reaction was terminated after the fourth iteration by stopping stirring followed by centrifugation, without further reagent addition.

For the preparation of S-GMNPs, the initial citrate concentration was increased to 227.27 μM, with each subsequent citrate addition raised to 100 μL. Conversely, for the preparation of L-GMNPs, the initial citrate concentration was lowered to 22.73 μM, and the citrate supplement was reduced to 10 μL.

4.4 Quantification of surface citrate loading on Fe_3O_4 nanoparticles by HPLC–DAD

Surface citrate loading on Fe_3O_4 nanoparticles was quantified by HPLC-DAD according to a previously reported RP-HPLC method with minor modifications[44]. Briefly, Fe_3O_4@citrate nanoparticles prepared with different citrate concentrations were collected by magnetic separation and washed thoroughly with deionized water to remove free citrate. The purified nanoparticles were then digested with hydrochloric acid to dissolve the iron oxide cores and release surface-bound citrate. After complete digestion, the solution was diluted to a fixed volume, centrifuged, and filtered through a 0.22 μm membrane before HPLC analysis. Citrate standards were measured under the same conditions to establish the calibration curve. HPLC–DAD analysis was performed using a reversed-phase C18 column with a phosphate buffer (pH 2.9 ± 0.1)/methanol mixture (97.5:2.5, v/v) as the mobile phase, a flow rate of 1.0 mL min^{-1}, and a detection wavelength of 210 nm. The citrate concentration in each digested sample was calculated from the corresponding peak area and corrected by the dilution factor to determine the actual citrate loading on Fe_3O_4 nanoparticles.

4.5 Density functional theory calculations

Density functional theory (DFT) calculations were performed using the Quantum ESPRESSO package[45–47] to investigate the adsorption behavior and interfacial electronic interactions between $AuCl_3$ and citrate-modified Fe_3O_4 surfaces. The exchange-correlation interaction was described using the generalized gradient approximation (GGA) with the Perdew-Burke-Ernzerhof (PBE) functional. Electron-ion interactions were treated using the projector augmented-wave (PAW) method, with a plane-wave kinetic energy cutoff of 500 eV. Spin-polarized calculations were conducted for all systems. The on-site Coulomb interaction of Fe 3d electrons was treated using the DFT+U method within the Dudarev scheme, with an effective Hubbard parameter (U_{eff}) of 5.3 eV.

The Fe_3O_4 slab model was constructed from the optimized bulk structure to simulate surface adsorption. A vacuum layer of approximately 10 Å was introduced along the surface-normal direction to minimize artificial interactions between periodic images. During geometry optimization, the bottom atomic layers of the slab were fixed to preserve a bulk-like environment, whereas the remaining atoms, including the citrate ligands and $AuCl_3$ molecule, were fully relaxed. Structural optimizations were performed using a quasi-Newton algorithm until the residual force on each atom was below 0.02 eV $Å^{-1}$, while the lattice parameters were kept fixed. A dipole correction was applied along the surface-normal direction to reduce artificial electrostatic interactions associated with the asymmetric slab configuration. The Brillouin zone was sampled using a Γ-centered 1 × 1 × 1 Monkhorst-Pack k-point mesh. Electronic occupations were treated using Methfessel-Paxton smearing with a width of 0.2 eV. The protonation state of citrate and the surface chemical environment of Fe_3O_4 were considered when interpreting the calculated adsorption behavior in relation to the experimental synthesis conditions (pH = 9.5). Under these

Just Accepted

alkaline conditions, free citrate predominantly exists in its triply deprotonated form (Cit^{3-}), while the Fe_3O_4 surface may contain hydroxylated and deprotonated surface sites depending on its local chemical environment. To evaluate the interfacial electronic redistribution induced by $AuCl_3$ adsorption, the charge density difference (Δρ) was calculated according to:

$$\Delta\rho = \rho_{AuCl_3/substrate} - \rho_{substrate} - \rho_{AuCl_3}$$

where $\rho_{AuCl_3/substrate}$, $\rho_{substrate}$, and ρ_{AuCl_3} represent the electron densities of the complete adsorption system, the citrate-modified Fe_3O_4 substrate, and the isolated $AuCl_3$ molecule, respectively. The electron densities of the constituent fragments were evaluated using consistent atomic geometries and computational settings. The plane-averaged charge density difference was further projected along the surface-normal direction to characterize electron accumulation and depletion across the interface. Projected density of states (PDOS) analysis was performed to investigate the electronic interactions between Au d and O p orbitals. Bader charge analysis was conducted to quantify the local charge redistribution at the interfacial active sites.

The adsorption energy (E_{ads}) of $AuCl_3$ on the citrate-modified Fe_3O_4 surface was calculated as:

$$E_{ads} = E_{AuCl_3/substrate} - E_{substrate} - E_{AuCl_3}$$

where $E_{AuCl_3/substrate}$, $E_{substrate}$, and E_{AuCl_3} represent the total energies of the complete adsorption system, the corresponding citrate-modified Fe_3O_4 substrate, and the isolated $AuCl_3$ molecule, respectively. A more negative adsorption energy indicates a more energetically favorable adsorption configuration within the adopted computational model and reference states. VESTA software was used to visualize the optimized structures and charge density difference distributions[48].

4.6 Modification of GMNPs with 4-MBA

The modification of GMNPs with 4-MBA was adapted from previously reported protocols with minor modifications[49]. The general method presented here is suitable for all different sized GMNPs with various 4-MBA loading concentrations. For M-GMNPs, 10^{-4} M is determined to be the optimized 4-MBA loading concentration.

To prepare GMNPs@4-MBA, 9 mL of the M-GMNPs solution was mixed with 1 mL of 10^{-3} M 4-MBA solution under vigorous stirring to allow ligand exchange for 24 h. The obtained M-GMNPs@4-MBA nanoparticles were washed twice with deionized water to remove excess 4-MBA and redispersed in 10 mL of deionized water for further use.

4.7 SERS performance of GMNPs

A 20 μL aliquot of the GMNPs@4-MBA solution was deposited onto a fluorine-treated silicon wafer and allowed to air-dry. SERS spectra were then acquired using a confocal Raman spectrometer equipped with a 785 nm laser source operated at 10 mW, and collected over the range of 600–1800 cm^{-1} with an integration time of 15 seconds, with the intensity at 1075 cm^{-1} measured for quantification. For magnetic enrichment, 1 mL of GMNPs@4-MBA solution was placed by side of a neodymium magnet for 20 minutes. After magnetic separation, the supernatant was discarded, and the enriched particles were re-dispersed in 0.5 mL of deionized water. A 20 μL portion of this suspension was then applied to a silicon wafer, air-dried, and subjected to Raman measurement under identical conditions. This protocol was applied consistently across all GMNPs@4-MBA sizes using the same measurement conditions.

4.8 Preparation of GMNPs@4-MBA modified with anti-CRP detection mAb (GMNPs@4-MBA@anti-CRP detection mAb)

The anti-CRP detection mAb modified GMNPs@4-MBA probes were prepared according to previously reported protocols with minor modifications[37, 38, 50]. For anti-CRP detection mAb conjugation, 5 mL of M-GMNPs@4-MBA were transferred into a 15 mL centrifuge tube, and the pH was adjusted to 8.2 with 0.2 M K_2CO_3 solution. Anti-CRP detection mAb were diluted to 0.2 mg mL^{-1} using 0.02 M borate buffer and then added to the M-GMNPs@4-MBA solution to reach a final concentration of 5–15 μg mL^{-1} (for M-GMNPs, 10 μg mL^{-1} is ultimately determined to be the optimized anti-CRP detection mAb loading concentration). The mixture was incubated at room temperature for 45 min. Subsequently, 0.25 mL of 10% (w/v) BSA solution was added and incubated for 2 h to block unreacted gold surfaces and prevent nonspecific binding. The solution was centrifuged at 6000 rpm for 10 min at 4 °C, and the supernatant containing unbound anti-CRP detection mAb and BSA was removed. Finally, the residue was resuspended in 0.5 mL of gold-label resuspension buffer (0.04% NaN_3, 2% sorbitol, 5% sucrose, 0.1% Tween 20, and 0.1% PEG 6000) to obtain GMNPs@4-MBA@anti-CRP detection mAb, which were stored at 4 °C for further use.

4.9 Construction of lateral flow strips

The assembly of lateral flow test strips was conducted with modifications based on previously reported immunochromatographic strip fabrication methods[51]. Briefly, a nitrocellulose membrane was affixed to the center of a polyvinyl chloride backing card. An absorbent pad was attached to the upper end of the backing card, overlapping the lower end of the nitrocellulose membrane by approximately 2 mm to ensure continuous fluid flow. The T line and C line were defined by dispensing diluted anti-CRP capture mAb at concentrations ranging from 0.5 to 1.5 mg mL^{-1} and goat anti-mouse IgG at 0.2 mg mL^{-1} onto the membrane using a membrane dispenser (for M-GMNPs, 1.0 mg mL^{-1} is ultimately determined to be the optimized anti-CRP capture mAb loading concentration at the T line). The assembled membrane was dried at 37 °C for several hours. Finally, the membrane sheet was cut into 4 mm wide strips using a strip cutter and stored in a desiccator until further use.

4.10 LFIA experiments based on different sized GMNPs

LFIA experiments based on GMNPs with different sizes were carried out following a previously reported protocol with slight modifications[40]. This general method was uniformly applied to all GMNP sizes (S-, M-, and L-). Specifically, 40 μL of M-GMNPs@4-MBA@anti-CRP detection mAb were mixed with 80 μL of CRP standard solution at various concentrations. After incubation for 5 minutes, the mixture was applied to the sample pad of the test strip. Driven by capillary force, the formed immunocomplexes migrated upward to the T line, where they bound to the immobilized anti-CRP capture mAb, producing a visible signal. Excess particles continued to flow to the C line, where they were captured by goat anti-mouse IgG, forming a

Just Accepted

secondary color band. After 15 minutes, the signal was recorded using a portable immunochromatographic strip reader.

4.11 Magnetic enrichment and SERS performance measurements of GMNPs-based LFIA

To evaluate the effect of magnetic enrichment on GMNPs-based LFIA system and its SERS performance, 40 μL of M-GMNPs@4-MBA@anti-CRP detection mAb were first mixed with 80 μL of CRP standard solutions with varying concentrations, and subjected to magnetic enrichment using a neodymium magnet for 20 minutes. After removing the supernatant, the enriched GMNP probes were re-dispersed in 60 μL of gold-label resuspension buffer. The resulting solution was then added onto the sample pad of the test strip for colorimetric detection. After 15 minutes of development, the colorimetric signal was recorded using a portable immunochromatographic reader.

Subsequently, SERS signals at the T line were acquired using a confocal Raman spectrometer equipped with a 785 nm laser. The laser power was set to 10 mW, and the spectra were collected in the range of 600–1800 cm^{-1} with an integration time of 15 seconds. Raman intensity at 1075 cm^{-1} was measured, and quantitative analysis was performed using the averaged signal from 10 randomly selected points along the centerline of the T line.

4.12 LFIA experiment based on 45 nm AuNPs

The synthesis of 45 nm AuNPs was performed according to a previously reported method with slight modifications[52]. Briefly, 2.352 mL of 25 mM $HAuCl_4$ was added to 200 mL of deionized water and heated to boiling. Then, 2.28 mL of 34 mM sodium citrate solution was rapidly introduced under vigorous stirring. The reaction was continued for 10 minutes to yield monodisperse AuNPs with an average diameter of ~45 nm. The conjugation of anti-CRP detection mAb to AuNPs followed the same protocol used for GMNPs.

Subsequently, 40 μL of AuNPs@anti-CRP detection mAb was mixed with 80 μL of CRP standard solution at varying concentrations. After a 5-minute incubation, the mixture was added onto the sample pad. Driven by capillary force, the formed immunocomplexes migrated toward the T line, where they bound to immobilized anti-CRP capture mAb, producing a visible color signal. Excess complexes were captured by the goat anti-mouse IgG at the C line. After 15 minutes, the signal was recorded using a portable immunochromatographic strip reader.

4.13 Specificity and stability tests of GMNPs-based LFIA system

To further assess the feasibility of the colorimetric and SERS dual-mode GMNPs-based LFIA sensing system, specificity tests were performed using four potential interfering substances (PCT, SAA, IL-6, and PDGF-BB). Positive and negative controls were prepared using solutions containing CRP (1000 ng mL^{-1}) and gold-label resuspension buffer without CRP, respectively.

To evaluate the stability of the GMNPs-based LFIA system, the lateral flow strips and GMNP probes were stored and tested every 7 days for a duration of one month[38]. The coefficient of variation (CV) was calculated to assess the stability of the GMNPs-based LFIA using the following formula:

$$CV = \frac{SD}{mean} \times 100\%$$

SD represents the respective standard deviation of the colorimetric optical densities and the SERS signal intensities at the T line, and mean represents the respective average value of the colorimetric optical densities and the SERS signal intensities at the T line.

Electronic Supplementary Material: Supplementary material (Figures S1–S19) is available in the online version of this article at https://doi.org/10.26599/NR.2026.94909306.

Data availability

All data needed to support the conclusions in the paper are presented in the manuscript and/or the Electronic Supplementary Material. Additional data related to this paper may be requested from the corresponding author upon request.

Acknowledgements

This work is granted by the National Natural Science Foundation of China (52502341), the National Key R&D Program of China (2024YFA1210700), the Frontier Fundamental Research Program of Jiangsu Province for Leading Technology (BK20222002), the Joint Open Research Fund of Suzhou Institute of Nanotechnology and Nano-bionics & Jiangsu Province Hospital and the Medical Engineering Translational Fund of Jiangsu Province Hospital (NM202403), and the Key Project of Jiangsu Province for Research and Development (BE2017763). The authors acknowledge Nanjing Research Center for Biomedical Electron Microscopy (NRC-BEM) for the permission to use their facilities. The authors acknowledge the Analysis and Testing Center of Southeast University for the permission to use their facilities.

Declaration of competing interest

All the contributing authors report no conflict of interests in this work.

Author contribution statement

W. Z.: Methodology, software, data curation, investigation, validation, formal analysis, visualization, writing – original draft. J. Y.: Methodology, data curation, investigation, validation, formal analysis, visualization, writing – original draft. H. Z.: Data curation, investigation, validation, formal analysis, visualization. M. P.: Formal analysis, writing – review & editing. Y. Z.: Investigation. X. D.: Investigation. S. L.: Investigation. J. L.: Formal analysis, visualization, resources. Z. G.: Funding acquisition, writing – review & editing. J. X.: Funding acquisition, writing – review & editing. Y. C.: Writing – review & editing. K. H.: Conceptualization, methodology, formal analysis, supervision, project administration, resources, writing – original draft, writing – review & editing. Y. L.: Conceptualization, methodology, formal analysis, supervision, funding acquisition, visualization, project administration, resources, writing – original draft, writing – review & editing. N. G.: Conceptualization, formal analysis, supervision, funding acquisition, project administration, resources, writing – original draft, writing – review & editing. All the authors have approved the final manuscript.

Informed consent

Not applicable.

Just Accepted

Ethics statement

Not applicable.

Use of AI statement

None.

References

[1] Das, P.; Fatehbasharzad, P.; Colombo, M.; Fiandra, L.; Prosperi, D. Multifunctional magnetic gold nanomaterials for cancer. *Trends Biotechnol.* **2019**, *37*, 995-1010.

[2] Lin, L. S.; Yang, X.; Zhou, Z.; Yang, Z.; Jacobson, O.; Liu, Y.; Yang, A.; Niu, G.; Song, J.; Yang, H. H.; Chen, X. Yolk-shell nanostructure: An ideal architecture to achieve harmonious integration of magnetic-plasmonic hybrid theranostic platform. *Adv. Mater.* **2017**, *29*, 1606681.

[3] Zhang, S.; Ghalandari, B.; Wang, A.; Li, S.; Chen, Y.; Wang, Q.; Jiang, L.; Ding, X. Superparamagnetic composite nanobeads anchored with molecular glues for ultrasensitive label-free proteomics. *Angew. Chem. Int. Ed.* **2023**, *62*, e202309806.

[4] Moraes Silva, S.; Tavallaie, R.; Sandiford, L.; Tilley, R. D.; Gooding, J. J. Gold coated magnetic nanoparticles: from preparation to surface modification for analytical and biomedical applications. *Chem. Commun.* **2016**, *52*, 7528-7540.

[5] Zou, Y.; Sun, Z.; Wang, Q.; Ju, Y.; Sun, N.; Yue, Q.; Deng, Y.; Liu, S.; Yang, S.; Wang, Z.; Li, F.; Hou, Y.; Deng, C.; Ling, D.; Deng, Y. Core-shell magnetic particles: tailored synthesis and applications. *Chem. Rev.* **2025**, *125*, 972-1048.

[6] Tran, V. T.; Kim, J.; Tufa, L. T.; Oh, S.; Kwon, J.; Lee, J. Magnetoplasmonic nanomaterials for biosensing/imaging and in vitro/in vivo biousability. *Anal. Chem.* **2018**, *90*, 225-239.

[7] Kwon, S. G.; Krylova, G.; Phillips, P. J.; Klie, R. F.; Chattopadhyay, S.; Shibata, T.; Bunel, E. E.; Liu, Y.; Prakapenka, V. B.; Lee, B.; Shevchenko, E. V. Heterogeneous nucleation and shape transformation of multicomponent metallic nanostructures. *Nat. Mater.* **2015**, *14*, 215-223.

[8] Lee, J.; Yang, J.; Kwon, S. G.; Hyeon, T. Nonclassical nucleation and growth of inorganic nanoparticles. *Nat. Rev. Mater.* **2016**, *1*, 16034.

[9] Zhu, Z.; Zhu, Y. Regulating surface faceting as a kinetic switch for core-shell nanoparticle crystallization pathways. *ACS Nano* **2026**, *20*, 11790-11800.

[10] Lo, C. K.; Xiao, D.; Choi, M. M. F. Homocysteine-protected gold-coated magnetic nanoparticles: synthesis and characterisation. *J. Mater. Chem.* **2007**, *17*, 2418-2427.

[11] Chen, H.; Qi, F.; Zhou, H.; Jia, S.; Gao, Y.; Koh, K.; Yin, Y. Fe_3O_4@Au nanoparticles as a means of signal enhancement in surface plasmon resonance spectroscopy for thrombin detection. *Sens. Actuators, B* **2015**, *212*, 505-511.

[12] Chuah, K.; Lai, L. M.; Goon, I. Y.; Parker, S. G.; Amal, R.; Justin Gooding, J. Ultrasensitive electrochemical detection of prostate-specific antigen (PSA) using gold-coated magnetic nanoparticles as 'dispersible electrodes'. *Chem. Commun.* **2012**, *48*, 3503-3505.

[13] Li, Z.; Fan, Q.; Wu, C.; Li, Y.; Cheng, C.; Yin, Y. Magnetically tunable plasmon coupling of Au nanoshells enabled by space-free confined growth. *Nano Lett.* **2020**, *20*, 8242-8249.

[14] Dong, W.; Li, Y.; Niu, D.; Ma, Z.; Gu, J.; Chen, Y.; Zhao, W.; Liu, X.; Liu, C.; Shi, J. Facile synthesis of monodisperse superparamagnetic Fe_3O_4 core@hybrid@Au shell nanocomposite for bimodal imaging and photothermal therapy. *Adv. Mater.* **2011**, *23*, 5392-5397.

[15] Ghosh, S.; Manna, L. The many "facets" of halide ions in the chemistry of colloidal inorganic nanocrystals. *Chem. Rev.* **2018**, *118*, 7804-7864.

[16] Li, C.; Shuford, K. L.; Chen, M.; Lee, E. J.; Cho, S. O. A facile polyol route to uniform gold octahedra with tailorable size and their optical properties. *ACS Nano* **2008**, *2*, 1760-1769.

[17] Chanana, M.; Liz-Marzán, L. M. Coating matters: the influence of coating materials on the optical properties of gold nanoparticles. *Nanophotonics* **2012**, *1*, 199-220.

[18] Personick, M. L.; Mirkin, C. A. Making sense of the mayhem behind shape control in the synthesis of gold nanoparticles. *J. Am. Chem. Soc.* **2013**, *135*, 18238-18247.

[19] Zhang, J.; Chen, Y.; Chen, Y.; Xiao, L. Ligand synergy and interfacial dynamics in multistep crystallization of indium nanocrystals. *Adv. Funct. Mater.* **2026**, *36*, e26879.

[20] Al-Johani, H.; Abou-Hamad, E.; Jedidi, A.; Widdifield, C. M.; Viger-Gravel, J.; Sangaru, S. S.; Gajan, D.; Anjum, D. H.; Ould-Chikh, S.; Hedhili, M. N.; Gurinov, A.; Kelly, M. J.; El Eter, M.; Cavallo, L.; Emsley, L.; Basset, J. M. The structure and binding mode of citrate in the stabilization of gold nanoparticles. *Nat. Chem.* **2017**, *9*, 890-895.

[21] Wuithschick, M.; Birnbaum, A.; Witte, S.; Sztucki, M.; Vainio, U.; Pinna, N.; Rademann, K.; Emmerling, F.; Kraehnert, R.; Polte, J. Turkevich in new robes: key questions answered for the most common gold nanoparticle synthesis. *ACS Nano* **2015**, *9*, 7052-7071.

[22] Zhang, Q.; Li, N.; Goebl, J.; Lu, Z.; Yin, Y. A systematic study of the synthesis of silver nanoplates: is citrate a "magic" reagent? *J. Am. Chem. Soc.* **2011**, *133*, 18931-18939.

[23] Lyon, J. L.; Fleming, D. A.; Stone, M. B.; Schiffer, P.; Williams, M. E. Synthesis of Fe oxide core/Au shell nanoparticles by iterative hydroxylamine seeding. *Nano Lett.* **2004**, *4*, 719-723.

[24] Huang, J.; Guo, M.; Ke, H.; Zong, C.; Ren, B.; Liu, G.; Shen, H.; Ma, Y.; Wang, X.; Zhang, H.; Deng, Z.; Chen, H.; Zhang, Z. Rational design and synthesis of γFe_2O_3@Au magnetic gold nanoflowers for efficient cancer theranostics. *Adv. Mater.* **2015**, *27*, 5049-5056.

[25] Zhang, X.; Chen, L.; Liu, R.; Li, D.; Ge, X.; Ge, G. The role of the OH group in citric acid in the coordination with Fe_3O_4 nanoparticles. *Langmuir* **2019**, *35*, 8325-8332.

[26] de Sousa, M. E.; Fernández van Raap, M. B.; Rivas, P. C.; Mendoza Zélis, P.; Girardin, P.; Pasquevich, G. A.; Alessandrini, J. L.; Muraca, D.; Sánchez, F. H. Stability and relaxation mechanisms of citric acid coated magnetite nanoparticles for magnetic hyperthermia. *J. Phys. Chem. C* **2013**, *117*, 5436-5445.

[27] Bastús, N. G.; Comenge, J.; Puntes, V. Kinetically controlled seeded growth synthesis of citrate-stabilized gold nanoparticles of up to 200 nm: size focusing versus Ostwald ripening. *Langmuir* **2011**, *27*, 11098-11105.

[28] Leng, Y.; Yin, X.; Hu, F.; Zou, Y.; Xing, X.; Li, B.; Guo, Y.; Ye, L.; Lu, Z. High-yield synthesis and fine-tuning aspect ratio of (200) faceted gold nanorods by the pH-adjusting method. *RSC Adv.* **2017**, *7*, 25469-25474.

[29] Li, T.; Cao, J.; Deng, Z.; Chen, Y.; Ye, Y.; Guo, Z.; Li, Y. Multidentate triazole coordination unlocks color-tunable plasmonic gold nanoparticle films to achieve high catalytic performance. *Small Methods* **2026**, *10*, e70847.

[30] Tyagi, H.; Kushwaha, A.; Kumar, A.; Aslam, M. A facile pH controlled citrate-based reduction method for gold nanoparticle synthesis at room temperature. *Nanoscale Res. Lett.* **2016**, *11*, 362.

Just Accepted

[31] Wang, W.; Hao, C.; Sun, M.; Xu, L.; Xu, C.; Kuang, H. Spiky Fe_3O_4@Au supraparticles for multimodal in vivo imaging. *Adv. Funct. Mater.* **2018**, *28*, 1800310.

[32] Cui, Y.; Hui, W.; Su, J.; Wang, Y.; Chen, C. Fe_3O_4/Au composite nano-particles and their optical properties. *Sci. China, Ser. B: Chem.* **2005**, *48*, 273-278.

[33] Leonel, A. G.; Mansur, H. S.; Mansur, A. A. P.; Caires, A.; Carvalho, S. M.; Krambrock, K.; Outon, L. E. F.; Ardisson, J. D. Synthesis and characterization of iron oxide nanoparticles/carboxymethyl cellulose core-shell nanohybrids for killing cancer cells in vitro. *Int. J. Biol. Macromol.* **2019**, *132*, 677-691.

[34] Gloag, L.; Mehdipour, M.; Chen, D.; Tilley, R. D.; Gooding, J. J. Advances in the application of magnetic nanoparticles for sensing. *Adv. Mater.* **2019**, *31*, 1904385.

[35] Hao, L.; Leng, Y.; Zeng, L.; Chen, X.; Chen, J.; Duan, H.; Huang, X.; Xiong, Y.; Chen, X. Core-shell-heterostructured magnetic-plasmonic nanoassemblies with highly retained magnetic-plasmonic activities for ultrasensitive bioanalysis in complex matrix. *Adv. Sci.* **2020**, *7*, 1902433.

[36] Shen, W.; Wang, C.; Yang, X.; Wang, C.; Zhou, Z.; Liu, X.; Xiao, R.; Gu, B.; Wang, S. Synthesis of raspberry-like nanogapped Fe_3O_4@Au nanocomposites for SERS-based lateral flow detection of multiple tumor biomarkers. *J. Mater. Chem. C* **2020**, *8*, 12854-12864.

[37] Chen, R.; Chen, X.; Zhou, Y.; Lin, T.; Leng, Y.; Huang, X.; Xiong, Y. "Three-in-one" multifunctional nanohybrids with colorimetric magnetic catalytic activities to enhance immunochromatographic diagnosis. *ACS Nano* **2022**, *16*, 3351-3361.

[38] Wang, C.; Cheng, Y.; Yin, X.; Wu, Q.; Ma, J.; Zhang, Q.; Zhao, L.; Wang, J.; Zhang, D. "Three-in-one": ultrasensitive lateral flow immunoassay driven by magnetic enrichment and photothermal signal amplification. *J. Agric. Food Chem.* **2024**, *72*, 18171-18180.

[39] Zhang, T.; Lei, L.; Tian, M.; Ren, J.; Lu, Z.; Liu, Y.; Liu, Y. Multifunctional Fe_3O_4@Au supraparticle as a promising thermal contrast for an ultrasensitive lateral flow immunoassay. *Talanta* **2021**, *222*, 121478.

[40] Liang, J.; Zeng, J.; Huang, X.; Zhu, T.; Gong, Y.; Dong, C.; Wang, X.; Zhao, L.; Xie, L.; Liang, K.; Tan, Q.; Cui, Y.; Kong, B.; Hui, W. Super-assembly of integrated gold magnetic assay with loop-mediated isothermal amplification for point-of-care testing. *Nano Res.* **2023**, *16*, 1242-1251.

[41] Liang, P.; Guo, Q.; Zhao, T.; Wen, C.-Y.; Tian, Z.; Shang, Y.; Xing, J.; Jiang, Y.; Zeng, J. Ag nanoparticles with ultrathin Au shell-based lateral flow immunoassay for colorimetric and SERS dual-mode detection of SARS-CoV-2 IgG. *Anal. Chem.* **2022**, *94*, 8466-8473.

[42] Zhou, H.; Kim, J. P.; Bahng, J. H.; Kotov, N. A.; Lee, J. Self‐assembly mechanism of spiky magnetoplasmonic supraparticles. *Adv. Funct. Mater.* **2014**, *24*, 1439-1448.

[43] Cui, Y.; Hu, D.; Fang, Y.; Ma, J. Preparation and mechanism of Fe_3O_4/Au core/shell super-paramagnetic microspheres. *Sci. China, Ser. B: Chem.* **2001**, *44*, 404-410.

[44] Matiushkina, A.; Abram, S. L.; Tavernaro, I.; Richstein, R.; Reithofer, M. R.; Andresen, E.; Michaelis, M.; Koch, M.; Resch-Genger, U. Quantifying citrate surface ligands on iron oxide nanoparticles with TGA, CHN analysis, NMR, and RP-HPLC with UV detection. *Anal. Chem.* **2025**, *97*, 19627-19634.

[45] Giannozzi, P.; Baroni, S.; Bonini, N.; Calandra, M.; Car, R.; Cavazzoni, C.; Ceresoli, D.; Chiarotti, G. L.; Cococcioni, M.; Dabo, I.; Dal Corso, A.; de Gironcoli, S.; Fabris, S.; Fratesi, G.; Gebauer, R.; Gerstmann, U.; Gougoussis, C.; Kokalj, A.; Lazzeri, M.; Martin-Samos, L.; Marzari, N.; Mauri, F.; Mazzarello, R.; Paolini, S.; Pasquarello, A.; Paulatto, L.; Sbraccia, C.; Scandolo, S.; Sclauzero, G.; Seitsonen, A. P.; Smogunov, A.; Umari, P.; Wentzcovitch, R. M. QUANTUM ESPRESSO: a modular and open-source software project for quantum simulations of materials. *J. Phys.: Condens. Matter* **2009**, *21*, 395502.

[46] Giannozzi, P.; Andreussi, O.; Brumme, T.; Bunau, O.; Buongiorno Nardelli, M.; Calandra, M.; Car, R.; Cavazzoni, C.; Ceresoli, D.; Cococcioni, M.; Colonna, N.; Carnimeo, I.; Dal Corso, A.; de Gironcoli, S.; Delugas, P.; DiStasio, R. A., Jr.; Ferretti, A.; Floris, A.; Fratesi, G.; Fugallo, G.; Gebauer, R.; Gerstmann, U.; Giustino, F.; Gorni, T.; Jia, J.; Kawamura, M.; Ko, H. Y.; Kokalj, A.; Kucukbenli, E.; Lazzeri, M.; Marsili, M.; Marzari, N.; Mauri, F.; Nguyen, N. L.; Nguyen, H. V.; Otero-de-la-Roza, A.; Paulatto, L.; Ponce, S.; Rocca, D.; Sabatini, R.; Santra, B.; Schlipf, M.; Seitsonen, A. P.; Smogunov, A.; Timrov, I.; Thonhauser, T.; Umari, P.; Vast, N.; Wu, X.; Baroni, S. Advanced capabilities for materials modelling with Quantum ESPRESSO. *J. Phys.: Condens. Matter* **2017**, *29*, 465901.

[47] Giannozzi, P.; Baseggio, O.; Bonfa, P.; Brunato, D.; Car, R.; Carnimeo, I.; Cavazzoni, C.; de Gironcoli, S.; Delugas, P.; Ferrari Ruffino, F.; Ferretti, A.; Marzari, N.; Timrov, I.; Urru, A.; Baroni, S. Quantum ESPRESSO toward the exascale. *J. Chem. Phys.* **2020**, *152*, 154105.

[48] Momma, K.; Izumi, F. VESTA 3 for three-dimensional visualization of crystal, volumetric and morphology data. *J. Appl. Cryst.* **2011**, *44*, 1272-1276.

[49] Zhu, C.-S.; Xiong, S.; Wang, C.; Dong, P.; Wu, X. SERS-based lateral flow immunoassay combined with enzymatic recombinase amplification for quantitative, high-sensitive detection of influenza A virus. *ACS Appl. Nano Mater.* **2024**, *7*, 3373-3384.

[50] Liu, J.; Guo, L.; Wu, A.; Song, S.; Liu, L.; Xu, C.; Kuang, H.; Xu, L. Immunochromatographic assay for the analysis of methomyl in cabbage and tomato. *Food Chem.* **2023**, *409*, 135273.

[51] Liu, J.; Li, L.; Li, H.; Sun, R.; Yin, H.; Sun, J. Ligand-assisted core-cavity-corona cubic plasmonic nanostructures amplify immunoassays for ultrasensitive triple-mode sensing of thrombomodulin. *Nano Res.* **2025**, *18*, 94907661.

[52] Si, K. J.; Sikdar, D.; Yap, L. W.; Foo, J. K. K.; Guo, P.; Shi, Q.; Premaratne, M.; Cheng, W. Dual‐coded plasmene nanosheets as next‐generation anticounterfeit security labels. *Adv. Optical Mater.* **2015**, *3*, 1710-1717.

© The Author(s) 20xx. *Nano Research* published by Tsinghua University Press. The articles published in this open access journal are distributed under the terms of the Creative Commons Attribution 4.0 International License (http://creativecommons.org/licenses/by/4.0/), which permits use, distribution and reproduction in any medium, provided the original work is properly cited.

Just Accepted

Electronic Supplementary Material

Ligand-programmed interfacial nucleation enables uniform ferrite-gold core-shell nanostructures

Weipeng Zhang [1], Jieyu Yan [2], Huanyu Zhao [1], Mingfei Pan [1], Yifan Zhao [3], Xuehuan Ding [1], Siyu Lin [1], Jizi Liu [3], Zhirui Guo [4], Jian Xu [5], Yi Chen [6], Kun Han [2] ✉, Yiyi Liu [1] ✉, Ning Gu [7,3] ✉

[1] Jiangsu Key Laboratory for Biomedical Electromagnetic Precision Theranostics, School of Biomedical Engineering and Informatics, Nanjing Medical University, Nanjing 211166, China
[2] CAS Key Lab of Bio-Medical Diagnostics, Suzhou Institute of Biomedical Engineering and Technology, Chinese Academy of Sciences, Suzhou 215163, China
[3] Nanjing Research Center for Biomedical Electron Microscopy (NRC-BEM), Nanjing Drum Tower Hospital, Medical School, Nanjing University, Nanjing 210093, China
[4] Nanobiotechnology Laboratory, The Second Affiliated Hospital of Nanjing Medical University, Nanjing 210029, China
[5] Department of Laboratory Medicine, The First Affiliated Hospital with Nanjing Medical University, Nanjing 210029, China
[6] Jiangsu Key Laboratory for Biomaterials and Devices, State Key Laboratory of Digital Medical Engineering, School of Biological Science and Medical Engineering, Southeast University, Nanjing 210096, China
[7] Jiangsu Key Laboratory for Cardiovascular Information and Health Engineering Medicine, Nanjing Drum Tower Hospital, Medical School, Nanjing University, Nanjing 210093, China

Supporting information to https://doi.org/10.26599/NR.2026.94909306

Just Accepted

Address correspondence to Kun Han, hank@sibet.ac.cn; Yiyi Liu, yiyi.liu@njmu.edu.cn; Ning Gu, guning@nju.edu.cn

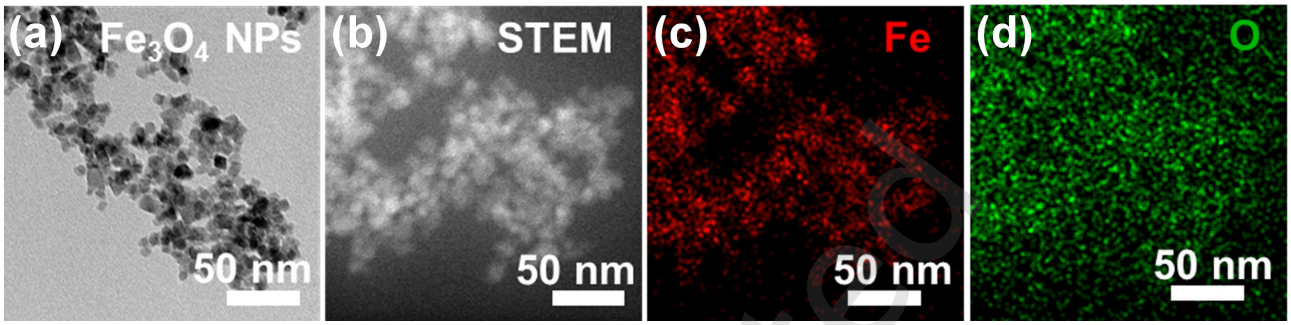


Figure S1. (a) TEM image, (b) STEM image and (c, d) EDS elemental mapping images of Fe_3O_4 nanoparticles.

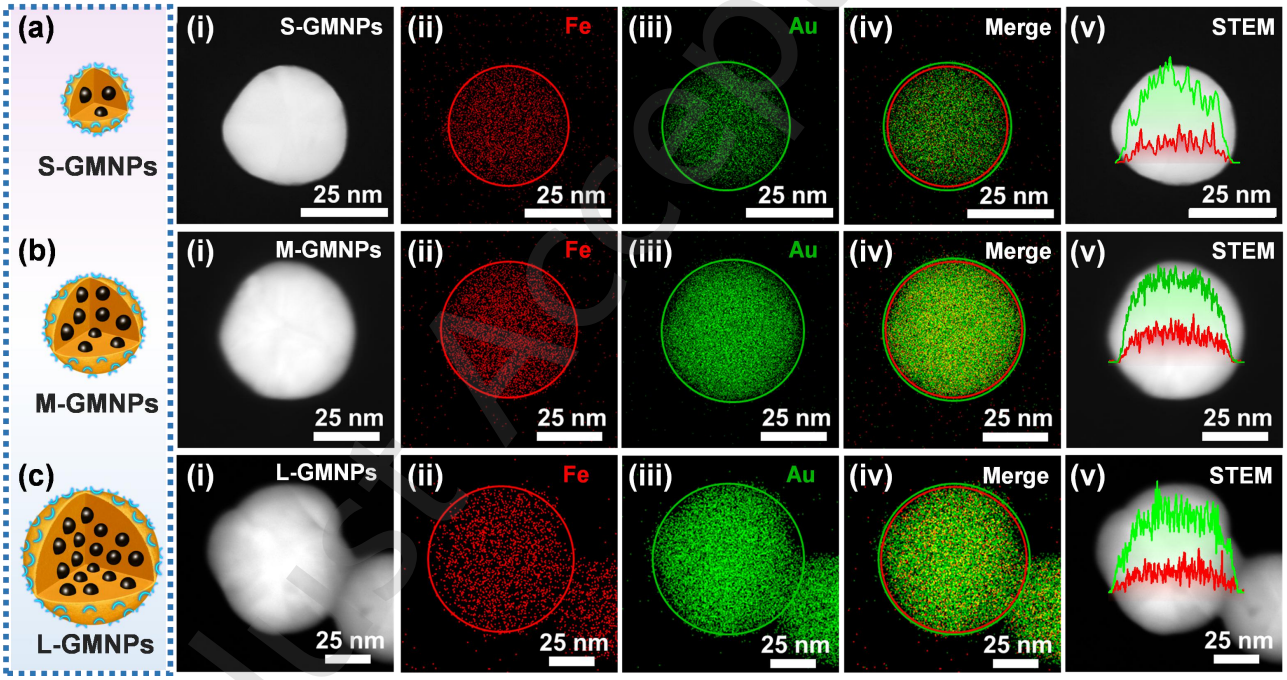


Figure S2. Schematic illustrations, STEM images, EDS elemental mapping images and line-scan profiles of (a) S-GMNPs, (b) M-GMNPs, and (c) L-GMNPs.

Just Accepted

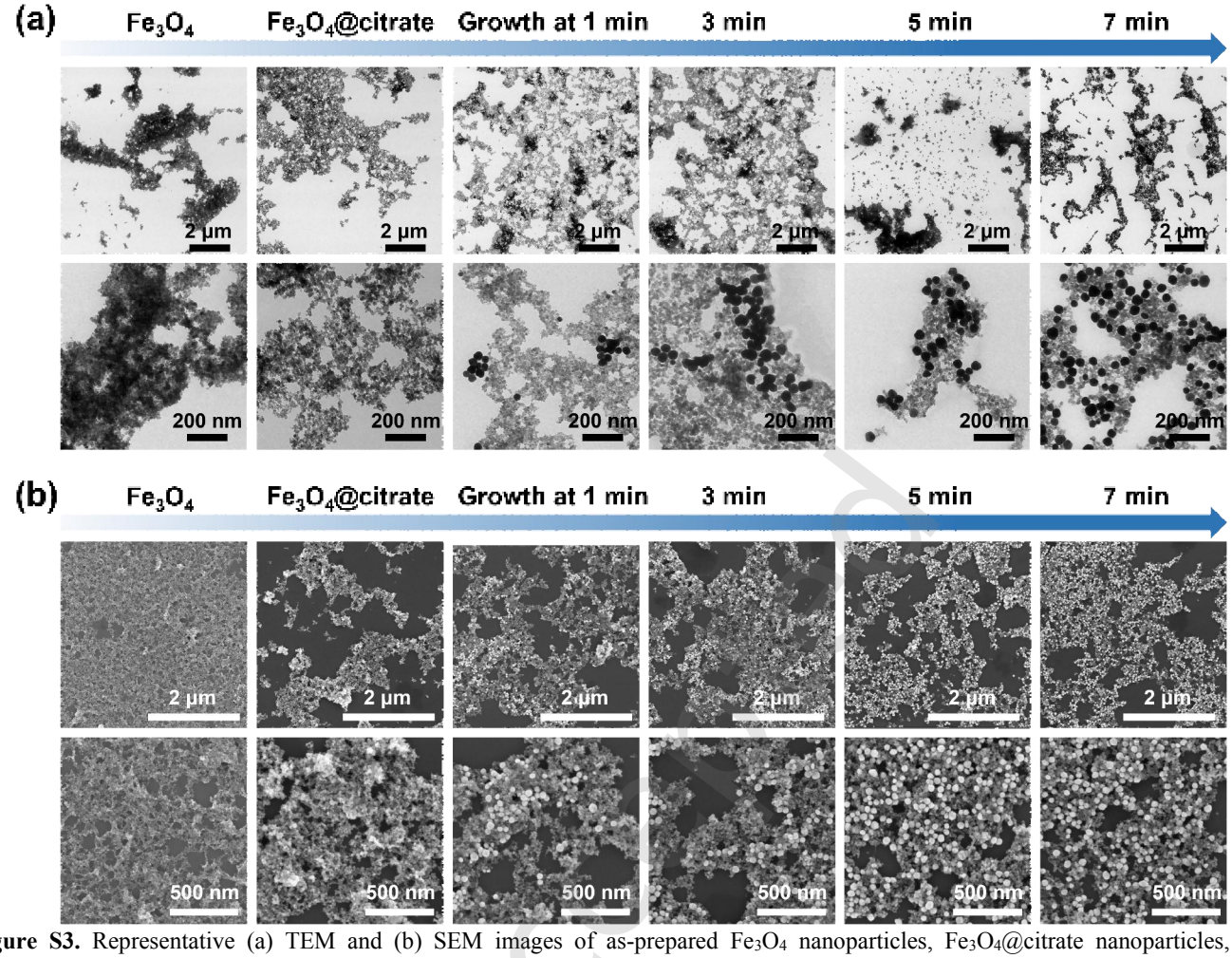


Figure S3. Representative (a) TEM and (b) SEM images of as-prepared Fe_3O_4 nanoparticles, Fe_3O_4@citrate nanoparticles, and samples of M-GMNPs collected at different stages from the initial gold growth (1, 3, 5, and 7 min) to before the first iterative coating cycle. The upper and lower rows in each panel show low- and high-magnification images, respectively.

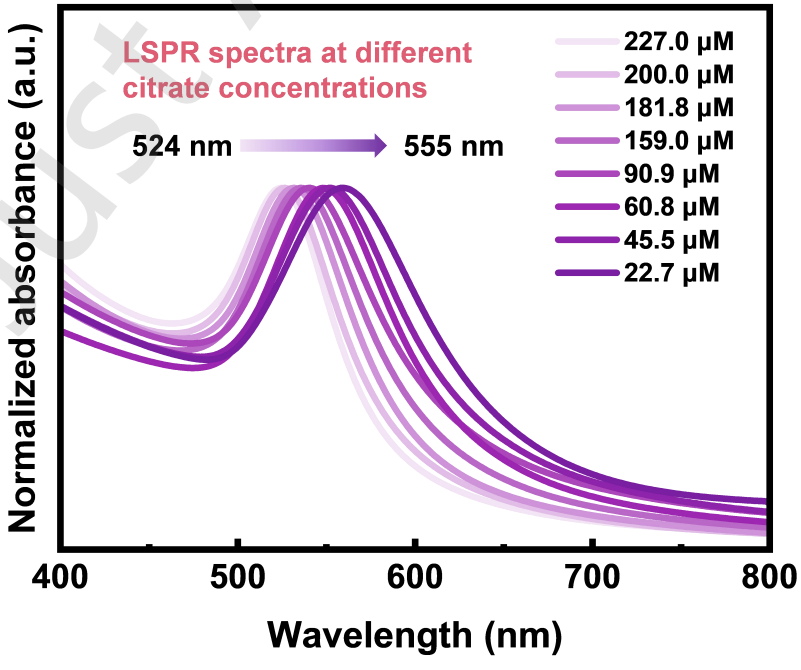


Figure S4. Normalized UV–vis absorption spectra of GMNPs prepared under different citrate concentrations, showing the LSPR peak positions redshift from 524 to 555 nm.

Just Accepted

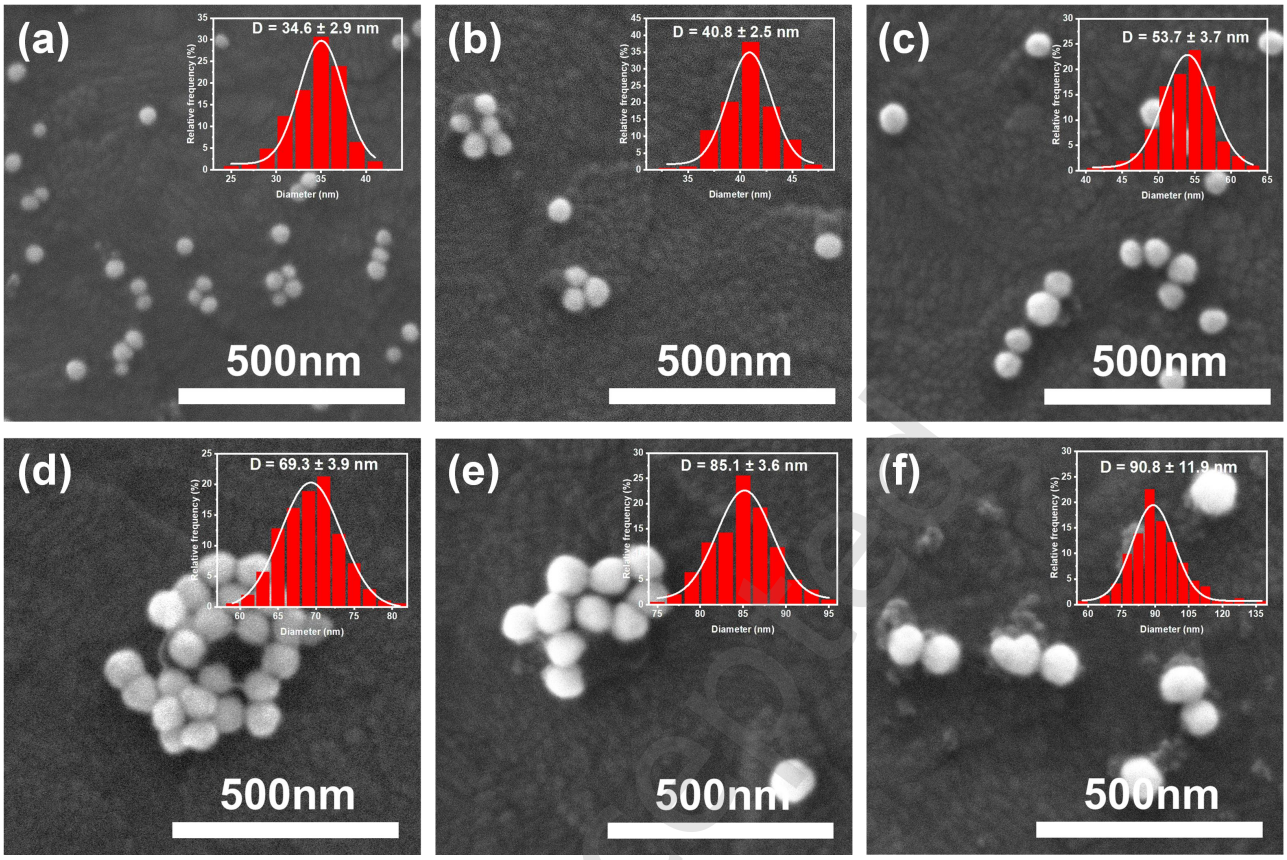


Figure S5. (a–f) SEM images of six different sized GMNPs. The inset in each SEM image shows the particle size distribution histogram determined from statistical analysis of 250 nanoparticles. The curve in each inset represents Gaussian fit of distribution.

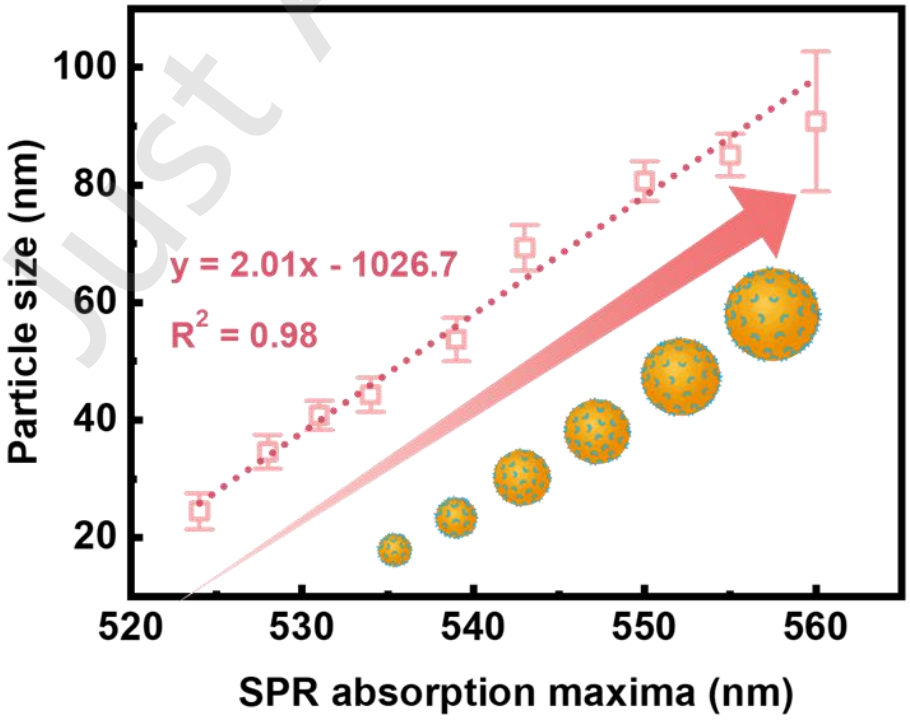
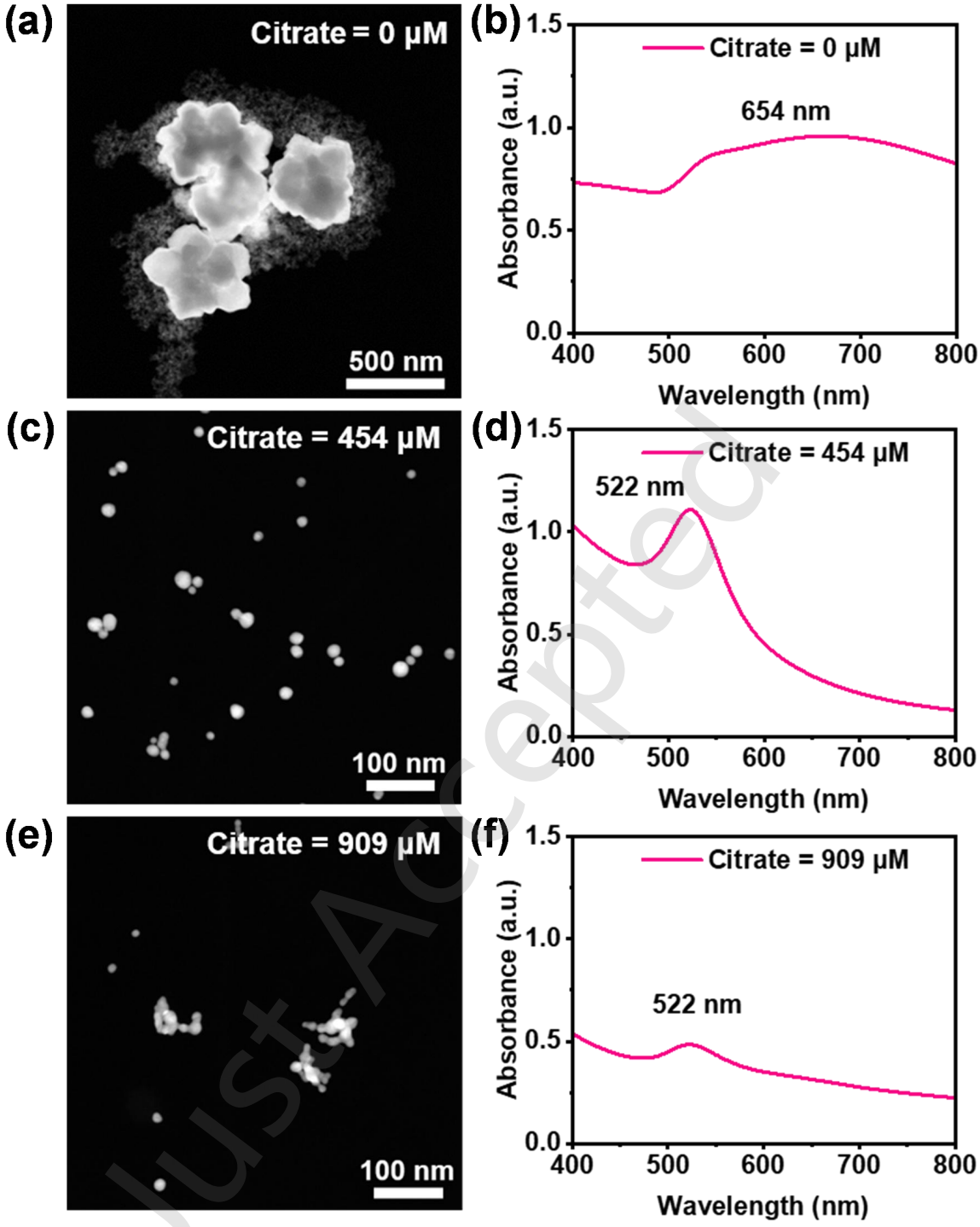


Figure S6. The linear correlation between GMNPs particle sizes and their corresponding LSPR peak positions, with an $R^2 = 0.98$.

Just Accepted



Just Accepted

Figure S7. (a) STEM image and (b) UV–vis absorption spectrum of GMNPs obtained without the presence of citrate. (c) STEM image and (d) UV–vis absorption spectrum of GMNPs obtained with the presence of excessive citrate (*i.e.*, 454 μM). (e) STEM image and (f) UV–vis absorption spectrum of GMNPs obtained with the presence of superfluous citrate (*i.e.*, 909 μM).

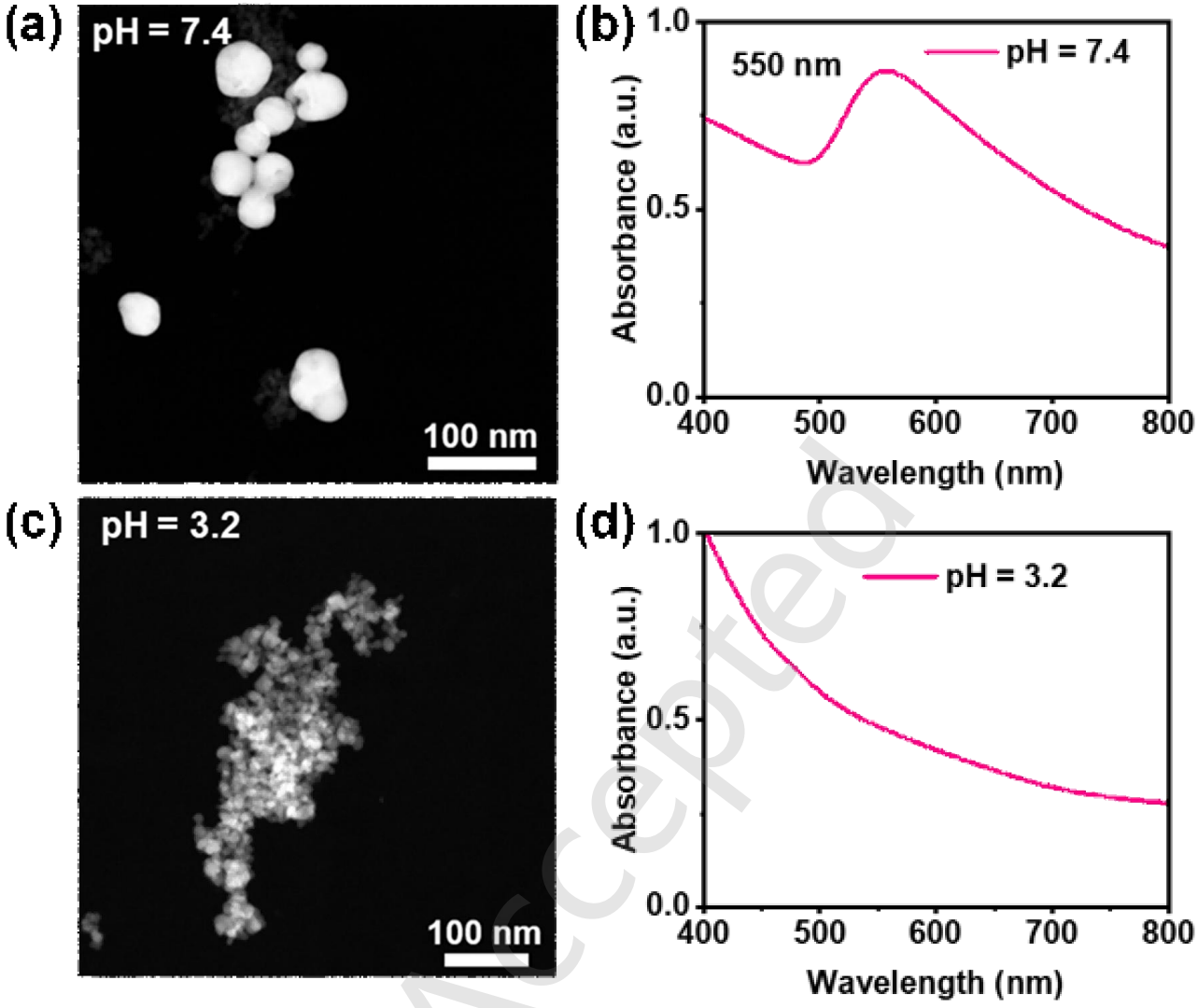


Figure S8. (a) STEM image and (b) UV–vis absorption spectrum of GMNPs prepared under neutral conditions (pH = 7.4, adjusted with 0.1 M HCl). (c) STEM image and (d) UV–vis absorption spectrum of GMNPs prepared under acidic conditions (pH = 3.2, adjusted with 0.1 M HCl).

Just Accepted

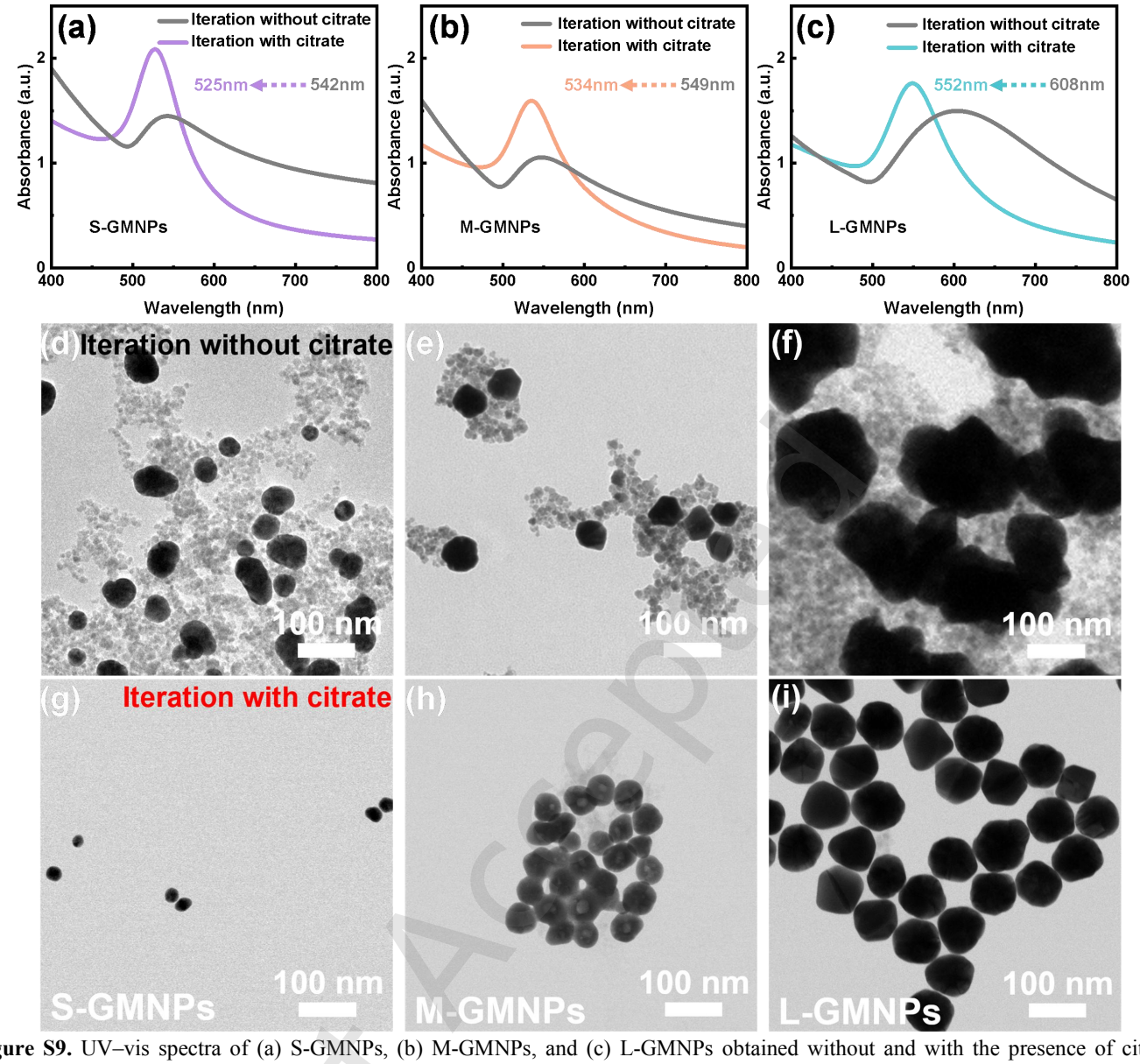


Figure S9. UV–vis spectra of (a) S-GMNPs, (b) M-GMNPs, and (c) L-GMNPs obtained without and with the presence of citrate during the iteration process. TEM images of (d) S-GMNPs, (e) M-GMNPs, and (f) L-GMNPs obtained without the presence of citrate during the iteration process. TEM images of (g) S-GMNPs, (h) M-GMNPs, and (i) L-GMNPs obtained with the presence of citrate during the iteration process.

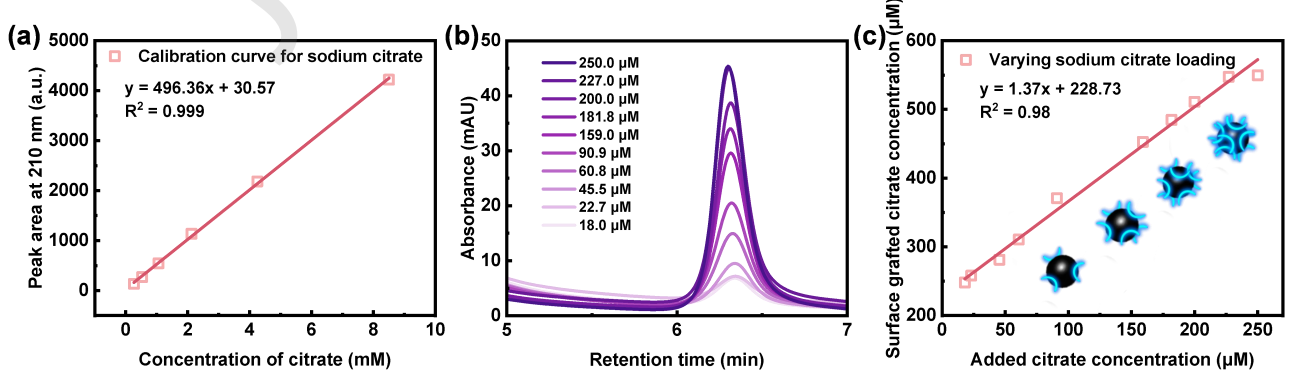


Figure S10. Quantification of citrate loading on Fe_3O_4 nanoparticles by HPLC–DAD. (a) Calibration curve of sodium citrate standards obtained from the peak area at 210 nm. (b) HPLC–DAD chromatograms of digested Fe_3O_4@citrate samples prepared with different citrate concentrations. (c) Correlation between surface grafted citrate concentration on Fe_3O_4 nanoparticles and added citrate concentration.

Just Accepted

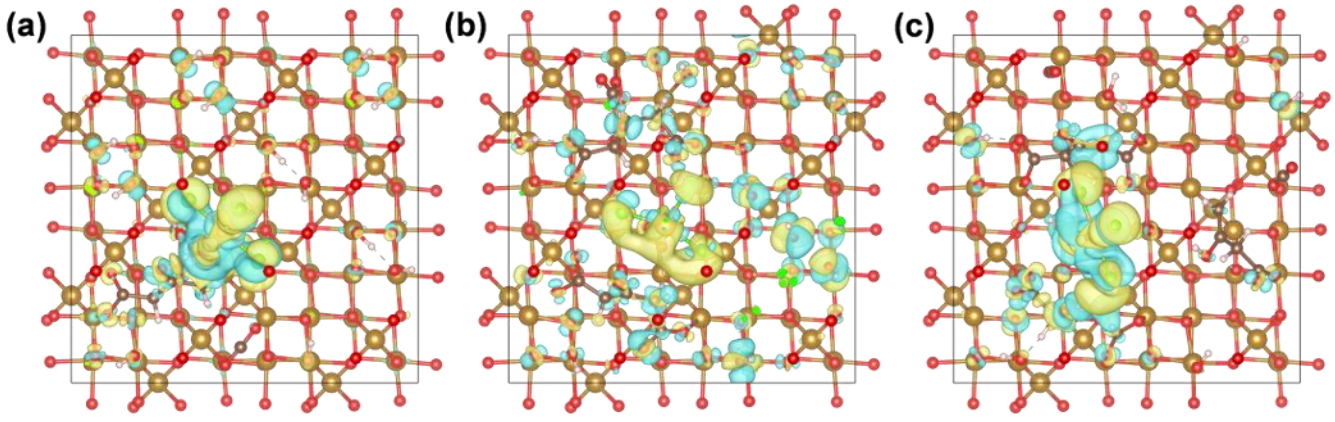


Figure S11. Top-view charge density difference maps of $AuCl_3$ adsorbed on citrate-modified Fe_3O_4 surfaces. (a–c) Top-view charge density difference maps of $AuCl_3$ adsorbed on Fe_3O_4 surfaces modified with 1, 2, and 3 citrate ligands, respectively. Yellow and cyan regions represent electron accumulation and depletion, respectively.

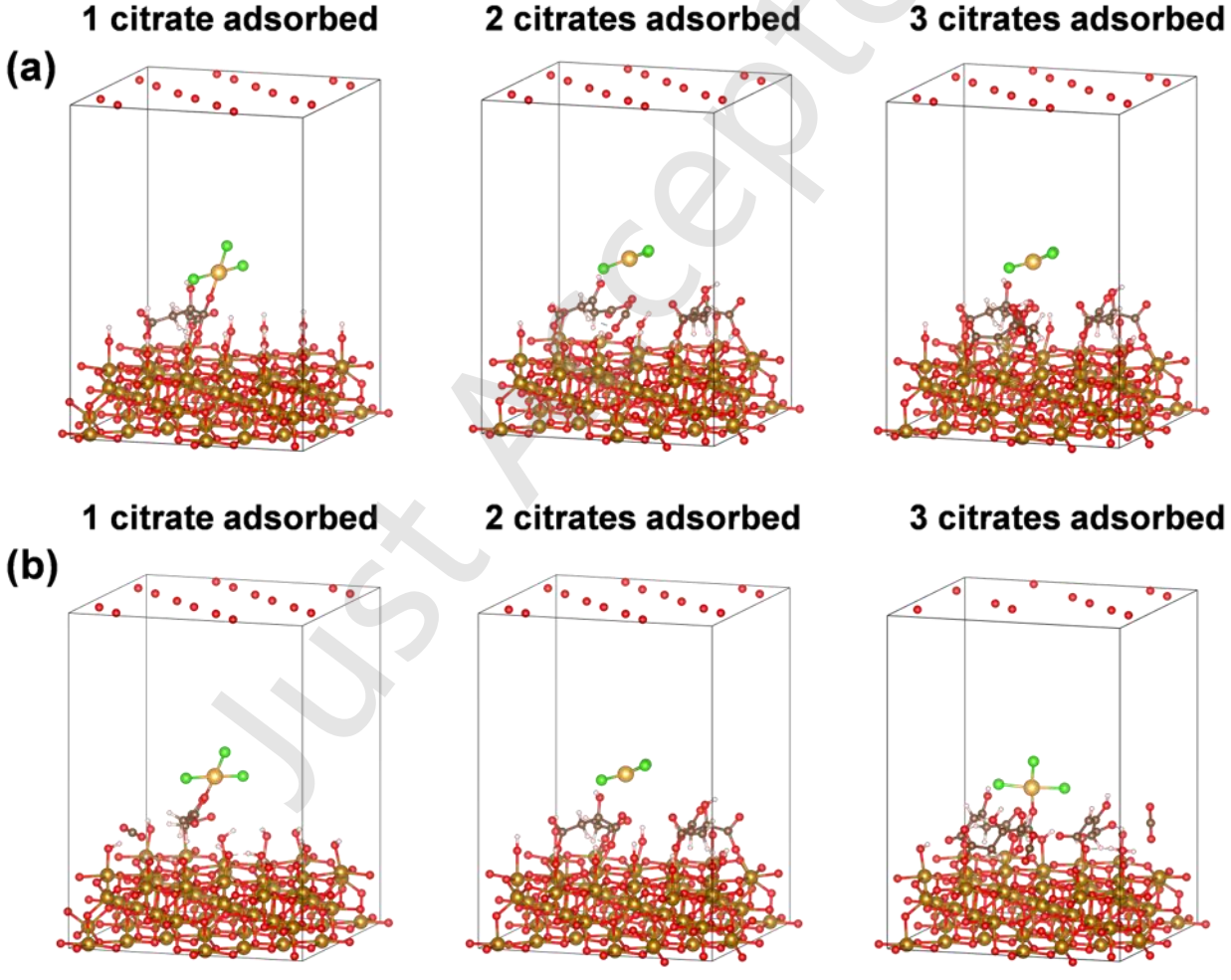


Figure S12. Initial and optimized adsorption configurations of $AuCl_3$ on citrate-modified Fe_3O_4 surfaces. (a) Initial structural models of $AuCl_3$ adsorbed on Fe_3O_4 surfaces modified with 1, 2, and 3 citrate ligands, respectively. (b) Optimized adsorption configurations of $AuCl_3$ on Fe_3O_4 surfaces modified with 1, 2, and 3 citrate ligands after DFT geometry optimization.

Just Accepted

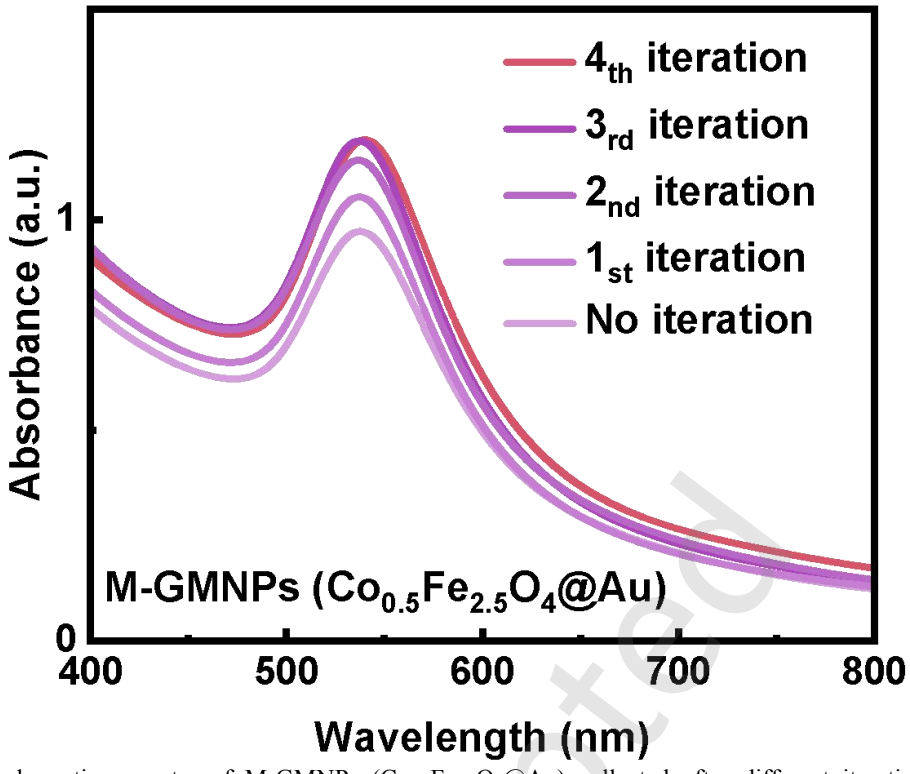


Figure S13. UV–vis absorption spectra of M-GMNPs ($Co_{0.5}Fe_{2.5}O_4$@Au) collected after different iterative additions of citrate, $HAuCl_4$, and hydroxylamine hydrochloride.

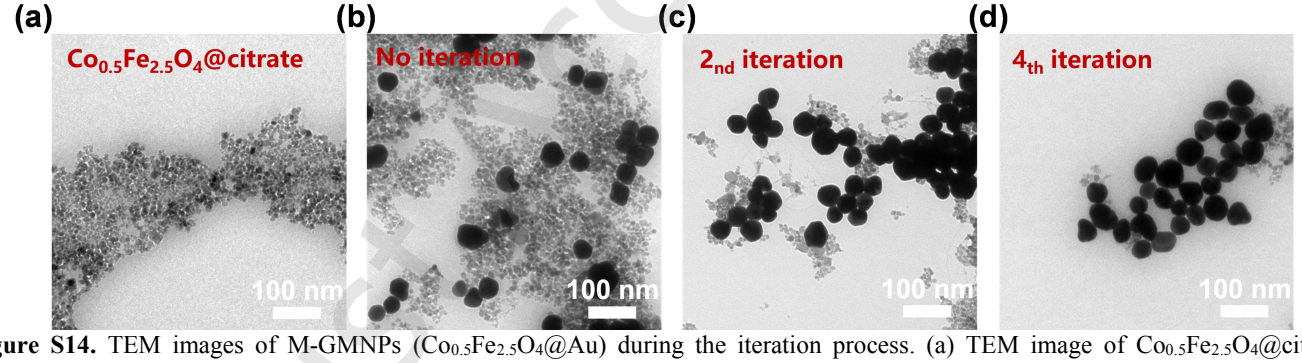


Figure S14. TEM images of M-GMNPs ($Co_{0.5}Fe_{2.5}O_4$@Au) during the iteration process. (a) TEM image of $Co_{0.5}Fe_{2.5}O_4$@citrate nanoparticles before gold deposition. (b–d) TEM images of M-GMNPs ($Co_{0.5}Fe_{2.5}O_4$@Au) obtained after no iteration, the 2nd iteration, and the 4th iteration, respectively.

Just Accepted

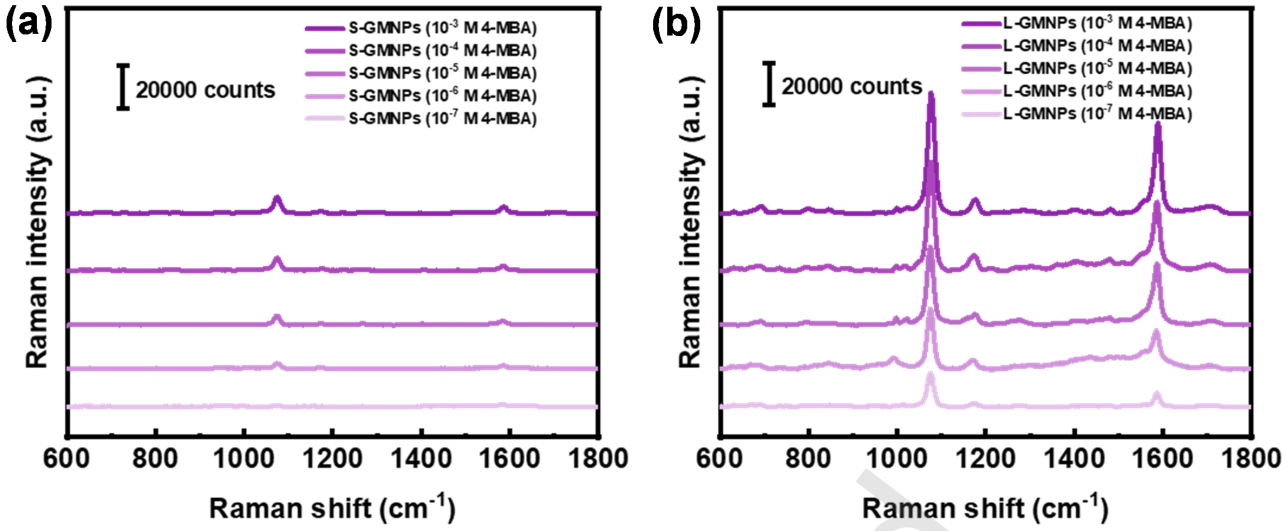


Figure S15. SERS spectra of 4-MBA on (a) S-GMNPs and (b) L-GMNPs with different loading concentrations (from 10^{-7} to 10^{-3} M) under natural drying.

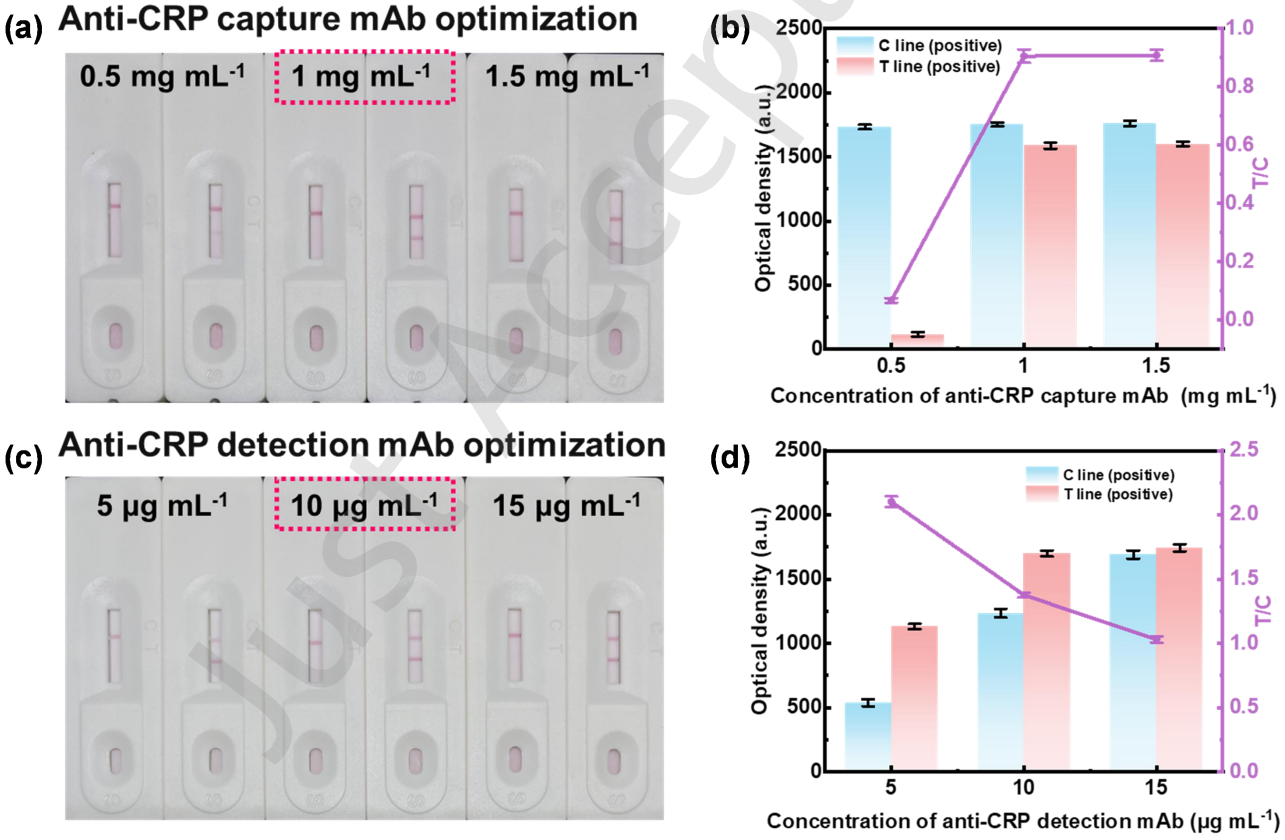


Figure S16. (a) Optical images and (b) the corresponding colorimetric responses of M-GMNPs-based LFIA strips in the detection of CRP with different anti-CRP capture mAb concentrations dispensing at the T line. (c) Optical images and (d) the corresponding colorimetric responses of M-GMNPs-based LFIA strips in the detection of CRP with M-GMNPs incubated with different concentrations of anti-CRP detection mAb.

Just Accepted

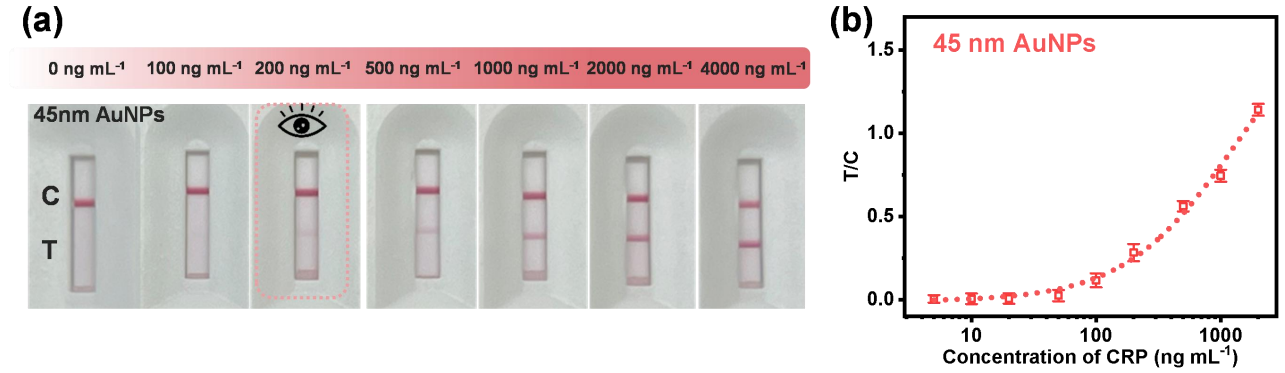


Figure S17. (a) Optical images of 45 nm AuNPs-based LFIA strips for CRP detection at different concentrations from 0 ng mL^{-1} to 4000 ng mL^{-1}. (b) Calibration curve of the corresponding colorimetric signals obtained from 45 nm AuNPs-based LFIA strips for CRP detection at different concentrations from 0 ng mL^{-1} to 2000 ng mL^{-1}.

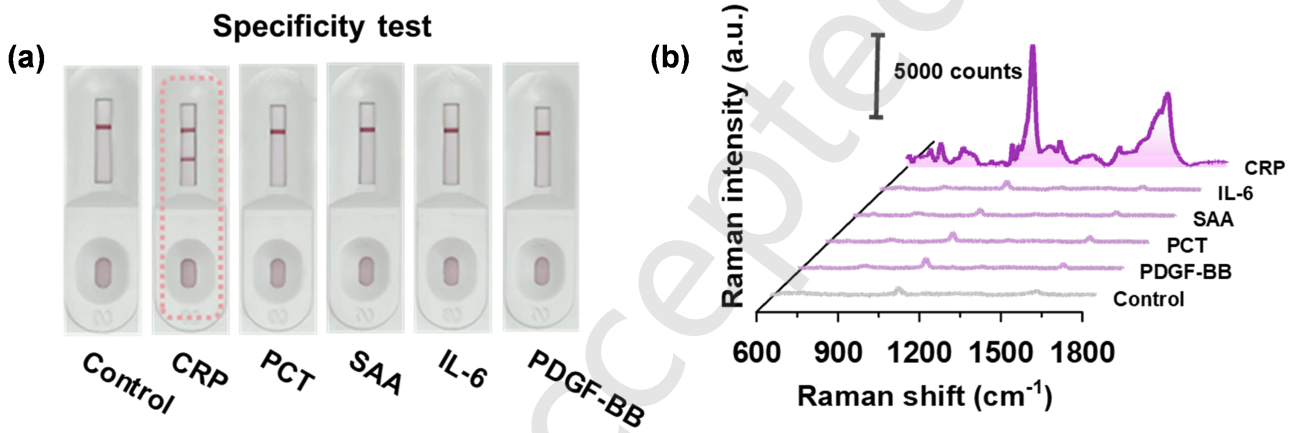


Figure S18. (a) Optical images of the specificity evaluation of M-GMNPs-based LFIA strips using CRP and four other inflammatory biomarkers. (b) SERS spectra collected at the T line of M-GMNPs-based LFIA strips corresponding to CRP and the other inflammatory biomarkers.

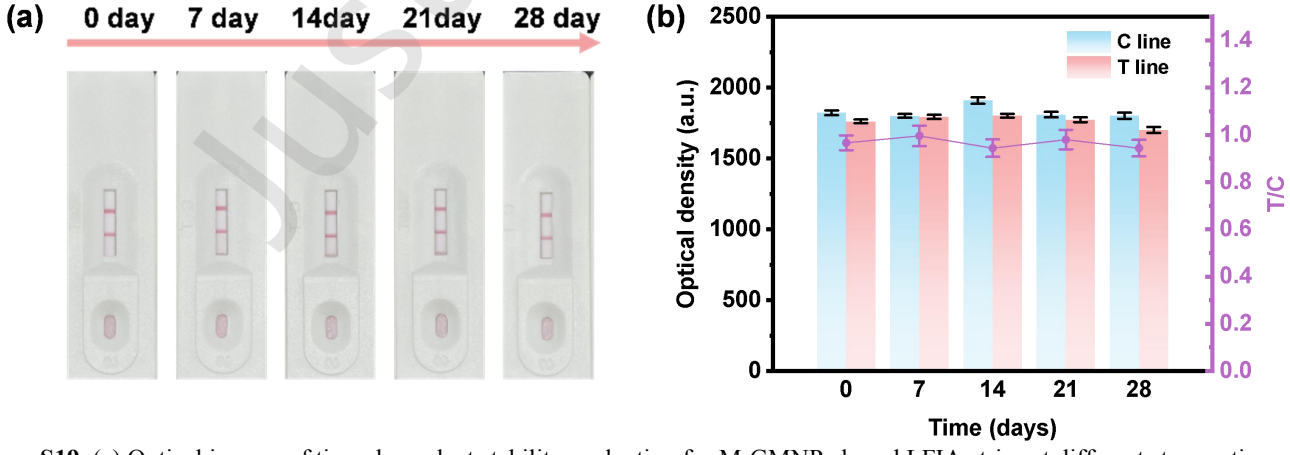


Figure S19. (a) Optical images of time-dependent stability evaluation for M-GMNPs-based LFIA strips at different storage times (0, 7, 14, 21, and 28 days). (b) Corresponding colorimetric signal intensities at the T line and C line of M-GMNPs-based LFIA strips at different storage times (0, 7, 14, 21, and 28 days).

Just Accepted